Secondary aerosol formation alters CCN activity in the North China Plain

Jiangchuan Tao[1, 2], Ye Kuang[1, 2], Nan Ma[1, 2], Juan Hong[1, 2], Yele Sun[3, 4, 5], Wanyun Xu[6], Yanyan Zhang[1], Yao He[3], Qingwei Luo[1], Linhong Xie[1, 2], Hang Su[7], Yafang Cheng[7]

[1]Institute for Environmental and Climate Research, Jinan University, Guangzhou, Guangdong 511443, China

[2]Guangdong-Hongkong-Macau Joint Laboratory of Collaborative Innovation for Environmental Quality, Guangzhou, China

[3]State Key Laboratory of Atmospheric Boundary Layer Physics and Atmospheric Chemistry, Institute of Atmospheric Physics, Chinese Academy of Sciences, Beijing 100029, China

[4]College of Earth and Planetary Sciences, University of Chinese Academy of Sciences, Beijing 100049, China

[5]Center for Excellence in Regional Atmospheric Environment, Institute of Urban Environment, Chinese Academy of Sciences, Xiamen 361021, China

[6]State Key Laboratory of Severe Weather, Key Laboratory for Atmospheric Chemistry, Institute of Atmospheric Composition, Chinese Academy of Meteorological Sciences, Beijing, 100081, china

[7]Multiphase Chemistry Department, Max Planck Institute for Chemistry, Mainz 55128, Germany

Correspondence to: Jiangchuan Tao (taojch@jnu.edu.cn) and Nan Ma (nan.ma@jnu.edu.cn)

Abstract:

Secondary aerosols (SA, including secondary organic and inorganic aerosols, SOA and SIA) are predominant components of aerosol particles in the North China Plain (NCP) and its formation has significant impacts on the evolution of particle size distribution (PNSD) and hygroscopicity. Previous studies have shown that distinct SA formation mechanisms can dominate under different relative humidity (RH). This would lead to different influences of SA formation on the aerosol hygroscopicity and PNSD under different RH conditions. Based on the measurements of size-resolved particle activation ratio (SPAR), hygroscopicity distribution (GF-PDF), $PM_{2.5}$ chemical composition, PNSD, meteorology and gaseous pollutants in a recent field campaign, McFAN (Multiphase chemistry experiment in Fogs and Aerosols in the North China Plain), conducted during the autumn-winter transition period in 2018 at a polluted rural site in the NCP, the influences of SA formation on cloud condensation nuclei (CCN) activity and CCN number concentration (N_{CCN}) calculation under different RH conditions were studied. Results suggest that during daytime, SA formation could lead to a significant increase in N_{CCN} and a strong diurnal variation in SPAR at Super-saturations lower than 0.07%. During periods with daytime minimum RH exceeding 50% (high RH conditions), SA formation significantly contributed to the particle mass/size changes in a broad size range of 150 nm to 1000 nm, led to N_{CCN}(0.05%) increases within the size range of 200 nm to 300 nm, and mass concentration growth mainly for particles larger than 300 nm. During periods with daytime minimum RH below 30% (low RH conditions), SA formation mainly contributed to the particle mass/size and N_{CCN} changes for particles smaller than 300 nm. As a result, under the same amount of mass increase induced by SA formation, the increase of N_{CCN}(0.05%) was stronger under low RH conditions and weaker under high RH conditions. Moreover, the diurnal variations of SPAR parameter (inferred from CCN measurements) due to SA formation varied with RH conditions, which was one of the largest uncertainties within N_{CCN} predictions. After considering the SPAR parameter (estimated through the number fraction of hygroscopic particles or mass fraction of SA), the relative deviation of N_{CCN}(0.05%) predictions were reduced to within 30%. This study highlights the impact of SA formation on CCN activity and N_{CCN} calculation, which provides guidance for future improvements of CCN predictions in chemical-transport models and climate models.

1. Introduction

Cloud condensation nuclei (CCN) activity of aerosol particles describes its ability to activate and grow into cloud droplets at given supersaturations and thus has important impacts on cloud microphysics and the aerosol indirect effect on climate. CCN activity is dependent on the physicochemical properties of aerosol particles, including particle size distributions, hygroscopicity (determined by chemical composition) and mixing state. Thus, atmospheric processes influencing these aerosol properties may exert influences on CCN activity.

Secondary aerosols (SA) formation contributes greatly to aerosol populations and impacts CCN properties in many ways, generally increasing CCN number concentrations (N_{CCN}) and leading to changes in the CCN activity (Wiedensohler et al., 2009; Kerminen et al., 2012; Wu et al., 2015; Farmer et al., 2015; Ma et al., 2016; Zhang et al., 2019 and reference therein). Differences in precursor and oxidant concentrations as well as SA formation mechanisms lead to particle size growth in different size ranges (Dal Maso et al., 2005; Kulmala et al., 2007; Zhang et al., 2012; Farmer et al., 2015; Cheng et al., 2016; Kuang et al., 2020c), thus would impact CCN activities in different ways. SA formation includes both the formation and subsequent growth of new particles (New Particle Formation, NPF), and the growth of existing particles. NPF can directly provide particles large enough to act as CCNs (Wiedensohler et al., 2009; Kerminen et al., 2012; Farmer et al., 2015), generally affecting aerosol particles smaller than 100 nm, thereby elevating N_{CCN} at higher supersaturations (SSs>0.2%) (Wiedensohler et al., 2009; Kerminen et al., 2012; Ma et al., 2016; Zhang et al., 2019 and reference therein). SA formation on existing particles, especially under polluted conditions, significantly adds mass to and changes the chemical composition of accumulation mode particles (Farmer et al., 2015), thus affecting CCN at lower SSs (<0.2%) (Wiedensohler et al., 2009; Mei et al., 2013; Yue et al., 2016; Thalman et al., 2017; Duan et al., 2018). SSs varies greatly among different clouds categories. Cumulus clouds are formed under higher SSs and are thus mostly influenced by Aitken mode particles formed in NPF events (Reuter et al., 2009; Gryspeerdt and Stier, 2012; Fan et al., 2016; Jia et al., 2019 and reference therein). Stratus clouds and fogs that exert stronger effects on climate and environment, however, are generally formed at SSs lower than 0.2%, indicating that only accumulation mode particles can serve as CCN (Ditas et al., 2012; Hammer et al., 2014a, b; Krüger et al., 2014; Shen et al., 2018). Numerous studies have investigated the impact of NPF on CCN (Gorden et al., 2016; Ma et al., 2016; Yu et al., 2020 and reference therein), however, only few studies have focused on the influence of SA formation on CCN activity of accumulation mode particles, which might exhibit strong climate and environment impacts and urgently requires attention.

80   SA formation affects CCN activity of accumulation mode particles not only by enlarging their

81   size, but also by changing their chemical compositions. At a specific particle size, the CCN activity is

82   determined both by the chemical composition of particles, which originally were and stayed this size,

83   and that of particles, which grew into this size via added SA mass. These two groups of particles can

84   exert different variations to CCN activity at the same particle size (Wiedensohler et al., 2009 and

85   reference therein). In general, the SA formation can increases the hygroscopicity of particles by adding

86   chemical compounds with lower volatility and higher oxidation state, which are usually more

87   hydrophilic, thereby enhancing CCN activity of accumulation mode particles (Mei et al., 2013; Yue et

88   al., 2016). However, CCN activity may also remain unchanged (Wiedensohler et al., 2009) or be

89   weakened in some cases (Thalman et al., 2017; Duan et al., 2018). In SA formation observed in central

90   Amazon forests, Thalman et al. (2017) reported enhanced CCN activity in dry season while constant

91   CCN activity in wet season. In SA formation events under polluted conditions in Guangzhou (Pearl

92   River Delta, China), Duan et al. (2018) found that bulk CCN activity can be enhanced in summer due

93   to the formation of large and inorganic-rich particles, but weakened in winter due to the formation of

94   small and organic-rich particles, where RH seemed to have been an important factor in the variations

95   of bulk CCN activity due to different particle formation pathways. Aside from variations of particle

96   chemical composition, changes in aerosol mixing states caused by SA formation can also change CCN

97   activity (Su et al., 2010; Rose et al., 2011; Cheng et al., 2012). The fast condensation of SA components

98   on accumulation mode particles led to the turnover of soot particle mixing state from externally to

99   internally mixed, which contributed mostly to enhancements of CCN activity (Cheng et al., 2012).

100 Thus, SA formation influences the CCN activity of accumulation mode particles through its integrated

101 impacts on their size, hygroscopicity and mixing state, which requires more detailed and

102 comprehensive investigations.

103 The North China Plain (NCP) frequently experiences severe aerosol pollution due to both

104 strong emissions of primary aerosol and strong SA formation caused by the abundance of gaseous

105 precursors and oxidants (Zheng et al. ACP, 2015; Liu et al., 2010; Huang et al., 2014; Xu et al., 2019).

106 In the SA formation events on the NCP, both aqueous-phase processes and gas-phase photochemical

107 processes can play important roles, depending on atmospheric conditions such as RH (Hu et al., 2016;

108 Xu et al., 2017a; Wang et al., 2019). A recent observational study on the NCP found that SA formation

109 dominantly contributed to different particle size since SA formation mechanisms varied with RH

110 conditions (Kuang et al., 2020c). Under dry conditions, SA were mainly formed through gas-phase

111 photochemical processing and mostly added mass to accumulation mode particles. While under high

112 RH conditions or super-saturated conditions, SA was also formed in aqueous phase, contributing to

113 the formation of both accumulation mode and coarse mode particles. The difference in particle size

114 where SA formation took place and the difference in SA chemical compositions could result in distinct

115 variations of CCN activity, which has not been evaluated yet. In this study, we will study the influence

116 of SA formation on Size-resolved Particle Activation Ratio (SPAR) of accumulation mode particles

117 in the NCP under different RH conditions, which fills a gap of knowledge within CCN studies in the

118 NCP and may provide guidance for the improvement of current CCN parameterization schemes in

119 chemical-transport and climate models.

120 **2. Method:**

121 2.1. Measurements

122 2.1.1. Site

123   Under the framework of McFAN (Multiphase chemistry experiment in Fogs and Aerosols in

124 the North China Plain) (Li et al., 2021), from 16th November to 16th December 2018, physical and

125 chemical properties of ambient aerosol particles as well as meteorological parameters were

126 continuously measured at the Gucheng site in Dingxing county, Hebei province, China. This site is an

127 Ecological and Agricultural Meteorology Station (39°09'N, 115°44'E) of the Chinese Academy of

128 Meteorological Sciences, which is located between Beijing (~100km) and Baoding (~40km), two

129 mega cities in the North China Plain, and surrounded by farmlands and small towns. Measurements at

130 this site can well represent the polluted background conditions of the NCP. All aerosol measurement

131 instruments were placed in a container with temperature maintained at 24 °C, while conventional trace

132 gas instruments including CO were housed in an air-conditioned room on a two-story building located

133 ~80 meters to the south of the container, with no taller buildings between them blocking the air flow.

134 2.1.2 Instrumentation

135   In this study, ambient aerosol was sampled by an inlet system consisting of a PM10 inlet

136 (Rupprecht & Patashnick Co., Inc., Thermo, 16.67 L/min), a Nafion dryer that dried relative humidity

137 to below 30% and an isokinetic flow splitter directing the air sample to each instrument.

138   A DMA-CCNC system measured SPAR at five supersaturations (SSs), 0.05%, 0.07%, 0.2%,

139 0.44% and 0.81%, with a running time of 20 min for 0.05% and 10 min for the other SSs. This system

140 consisted of a differential mobility analyzer (DMA model 3081; TSI, Inc, MN USA), a condensation

141 particle counter (CPC model 3772; TSI, Inc., MN USA) and a continuous-flow CCN counter (model

142 CCN200, Droplet Measurement Technologies, USA; Roberts and Nenes, 2005). The system was

143 operated in a size-scanning mode over the particle size range from 9 to 400 nm. SPAR can be obtained

144 by combining the measurements of CPC and CCNC at different particle size. The sample and sheath

flow rate of the DMA were set to 1 lpm and 5 lpm, respectively, hence the resultant measured particle diameter ranged from 9 nm to 500 nm. Since the low number concentration of particles above 300 nm could lead to large uncertainty in CCNC counting, the measurements for particles larger than 300 nm were excluded, except for 0.05% SS. In order to characterize the variations of particles with low hygroscopicity of about 0.1, SPAR measurement up to about 400 nm is used at 0.05% SS. There are 12 size distribution scans during a complete 1-hour cycle, with four scans for first SS and two scans for each of the rest four SSs. Only the last scan for each SS is used as the CCNC needs time for SS stabilization. The SSs of CCNC were calibrated with monodispersed ammonium sulphate particles (Rose et al., 2008) both before and after the campaign. The flowrates were checked regularly (every few days) during the campaign, as the flows (sample flow and sheath flow) of the instrument can affect both the counting of droplets and the SS in the column. A modified algorithm based on Hagen and Alofs (1983) and Deng et al. (2011, 2013) was used to correct the influence of multiple-charge particles and DMA transfer function on SPAR. Details about the system are described in Ma et al. (2016) and the description about the inversion method can be found in the supplements.

Non-refractory particulate matter (NR-PM) including SO_4^{2-}, NO_3^-, NH_4^+, Cl^- and organics with dry aerodynamic diameters below 2.5 μm was measured by an Aerodyne Time-of-Flight Aerosol Chemical Speciation Monitor (ToF-ACSM hereafter) equipped with a $PM_{2.5}$ aerodynamic lens (Williams et al., 2010) and a capture vaporizer (Xu et al., 2017b; Hu et al., 2017a) at 2-minute time resolution. The ToF-ACSM data were analyzed with the standard data analysis software (Tofware v2.5.13; https://sites.google.com/site/ariacsm/, last access: 21 January 2020). The organic mass spectra from m/z 12 to 214 were analyzed with an Igor Pro based positive matrix factorization (PMF) evaluation tool (v3.04) and then evaluated following the procedures described in Zhang et al. (2011). The chosen five-factor solution includes four primary factors i.e. hydrocarbon-like OA (HOA), cooking OA (COA), biomass burning OA (BBOA), and coal combustion OA (CCOA), and a secondary factor, i.e. oxygenated OA (OOA). More detailed descriptions on the ACSM measurements and data analysis can be found in Kuang et al. (2020b) and Sun et al. (2020).

A Humidified Tandem differential mobility analyzer (HTDMA, Tan et al., 2013) measured the size-resolved aerosol growth factor (GF) at 90% RH. The sampled particles were subsequently charged by a neutralizer (Kr85, TSI Inc.) and size selected by a DMA (DMA1, model 3081L, TSI Inc.). A Nafion humidifier (model PD-70T-24ss, Perma Pure Inc., USA) was used to humidify the monodisperse particles with a specific diameter (D_d) at a fixed RH of (90 ± 0.44) % and then the number size distribution of the humidified particles (D_{wet}) was measured by another DMA (DMA2,

model 3081L, TSI Inc.) and a condensation particle counter (CPC, model 3772, TSI Inc.). Thus, GF of the particles can be calculated as:

$$GF = \frac{D_{wet}}{D_d} \tag{1}$$

During the campaign, four dry mobility diameters (60, 100, 150, and 200 nm) were selected for the HTDMA measurements. A full scan takes about 1 hour in order to cover the four sizes. Regular calibration by using standard polystyrene latex spheres and ammonium sulfate were performed to ensure the instrument functioned normally. The tandem differential mobility analyzer (TDMA) inversion algorithm (Gysel et al., 2009) was applied to calculate the Probability Density Function of GF (GF-PDF). More details about this system can be found in Cai et al. (2018) and Hong et al. (2018).

Particle number size distributions (PNSDs) were measured by combining the measurements of a scanning mobility particle sizer (SMPS, TSI model 3080) and an aerodynamic particle sizer (APS, TSI Inc., Model 3321), that measured particle mobility diameter size distributions in the range of 12 nm to 760 nm and particle aerodynamic diameter size distribution in the range of 700 nm to 10 μm, respectively. A commercial instrument from Thermo Electronics (Model 48C) was used to measure CO concentration. Besides monthly multipoint calibrations and weekly zero-span check, additional 6-hourly zero checks were also performed for the CO instrument.

2.2. Data processing

2.2.1. Aerosol hygroscopicity and cloud activation: κ-Köhler theory

The ability of particles to act as CCN and its dependence on particle size and particle chemical composition on CCN activity can be described by the Köhler theory (Köhler, 1936). A hygroscopic parameter κ is calculated based on the κ-Köhler theory (Petters and Kreidenweis. 2007) to evaluate the influence of particle chemical compositions:

$$\kappa = \left(\frac{D_{wet}^3 - D_d^3}{D_d^3}\right) \left[\frac{1}{S}\exp\left(\frac{4\sigma_{s/a}M_w}{RT\rho_w D_{wet}}\right) - 1\right], \tag{1}$$

where S represents the saturation ratio, ρ_w is the density of water, M_w is the molecular weight of water, $\sigma_{s/a}$ is the surface tension of the solution/air interface, R is the universal gas constant, T is the temperature, D_d is the diameter of dry particle and D_{wet} is the diameter of the humidified particle. In this study, $\sigma_{s/a}$ is assumed to be the surface tension of pure water/air interface. Based on the κ-Köhler theory, the surface equilibrium water vapor saturation ratio of particles with a specific κ at different wet particle size can be calculated, and the maximum value of surface equilibrium saturation ratio (which is generally supersaturated) is defined as the critical SS for CCN activation. As a result, the

207 variation of the critical diameter (D_a) for particles with different hygroscopicity (or GF at a specific

208 RH) at different SSs can be determined.

209 2.2.2. Aerosol growth factor and its probability density function

210   In practice, the growth factor probability density function (GF-PDF) was inversed from the

211 measured GF distribution using a TDMAinv algorithm (Gysel et al., 2009). After obtaining the GF-

212 PDF, the ensemble average GF and corresponding critical diameter under a certain SS ($D_{a,GF}$) can be

213 calculated. Furthermore, the number fraction and the weighted-average GF of hygroscopic particles

214 ($\kappa > 0.1$ and GF(90%, 200 nm)>1.22) were calculated as:

$$\text{NF}_{\text{hygro}} = \int_{1.2}^{\infty} \text{PDF(GF)} \times d\text{GF} \quad\quad (2)$$

$$\text{GF}_{\text{hygro}} = \int_{1.2}^{\infty} \text{GF} \times \text{PDF(GF)} \times d\text{GF} \quad\quad (3)$$

217 Based on the κ-Köhler theory, the hygroscopicity parameter κ and corresponding critical diameter

218 ($D_{a,\text{hygro}}$) under a certain SS for particles with GF_{hygro} can be calculated. As GF_{hygro} is higher than the

219 average GF, $D_{a,\text{hygro}}$ is smaller than $D_{a,GF}$.

220 2.2.3 Calculations of aerosol hygroscopicity from aerosol chemical-composition measurements

221   For the calculation of aerosol hygroscopicity parameter κ based on measured chemical

222 composition data (κ_{chem}), detailed information on the chemical species are needed. The ACSM can

223 only provide bulk mass concentrations of SO_4^{2-}, NO_3^-, NH_4^+, Cl^- ions and organic components, which

224 cannot be used to calculate size resolved hygroscopicity. However, in the North China Plain,

225 accumulation mode particles are the dominant contributors to the bulk particle mass concentration (Liu

226 et al., 2014; Xu et al., 2015; Hu et al., 2017b) and thus the bulk chemical compositions can be used as

227 a proxy for that of accumulation mode particles. For the inorganic ions, a simplified ion pairing scheme

228 was used to convert ion mass concentrations to mass concentrations of corresponding inorganic salts

229 (Gysel et al., 2007; Wu et al., 2016). Thus, mass concentrations of SO_4^{2-}, NO_3^-, NH_4^+ and Cl^- are

230 specified into ammonium sulfate (AS), ammonium nitrate (AN), ammonium chloride (AC) and

231 ammonium bisulfate (ABS), for which the κ values under super-saturated conditions were specified

232 according to Petters and Kreidenweis (2007). For a given internal mixture of different aerosol chemical

233 species, the Zdanovskii–Stokes–Robinson (ZSR) mixing rule can be applied to predict the overall κ_{chem}

234 using volume fractions of each chemical species (ε_i) (Petters and Kreidenweis, 2007):

$$\kappa_{\text{chem}} = \sum_i \kappa_i \cdot \varepsilon_i \quad\quad (4)$$

236 where κ_i and ε_i represent the hygroscopicity parameter κ and volume fraction of chemical component
237 i in the mixture. Based on Eq.2, κ_{chem} can be calculated as follows:

$$\kappa_{chem}=\kappa_{AS}\varepsilon_{AS}+ \kappa_{AN}\varepsilon_{AN}+\kappa_{ABS}\varepsilon_{ABS}+\kappa_{AC}\varepsilon_{AC}+\kappa_{BC}\varepsilon_{BC}+\kappa_{Org}\varepsilon_{Org} \qquad (5)$$

239 where κ_{BC} is assumed to be zero as black carbon is non-hygroscopic~~hydrophilic~~. κ_{org} and ε_{org} represent
240 κ and volume fraction of total organics. The values of hygroscopicity parameter for inorganic
241 compounds can be found in Table 1 of Kuang et al. (2020b). Large variations in κ_{org} has been reported
242 in former studies and a linear relationship between κ_{org} and organic aerosol oxidation state (f44) was
243 detected in our campaign (Kuang et al., 2020b), which was adopted to calculate κ_{org} in this study:

$$\kappa_{Org}=1.04\times f44-0.02 \qquad (6)$$

245   It should be noted that the κ-Köhler theory is not perfect, even for inorganic compounds.
246 Numerous studies have been focusing on the performance of its application on measurements under
247 different RH conditions (Liu et al., 2011; Wang et al., 2017). And κ_{org} used in this study was
248 determined by the measurement of humidified nephelometer at RH of 85% in Petters and Kreidenweis,
249 (2007), due to the lack of κ_{org} measured under super-saturated conditions. In this study, we focus on
250 the variations of κ values derived from HTDMA and CCN measurement during the SA formation
251 events, rather than the closure between κ values derived using different techniques, which will be
252 addressed in an upcoming study.

253 2.2.4. Fitting parameterization scheme of SPAR

254   In general, the variation in CCN activity of a particle population can be attributed to the
255 variation in the number fraction of hygroscopic particles or its hygroscopicity, which can be indicated
256 by fitting parameters of SPAR curves parameterization. SPAR curves are often parameterized using a
257 sigmoidal function with three parameters. This parameterization assumes aerosols to be an external
258 mixture of apparently hygroscopic particles that can act as CCN and non-hygroscopic particles that
259 cannot be measured by CCNC within the measured particle size range below 400 nm (Rose et al.,
260 2010). SPAR ($Ra(D_p)$) at a specific SS can be described as follows (Rose et al., 2008):

$$Ra(D_p)=\frac{MAF}{2}\left(1+erf\left(\frac{D_p-D_a}{\sqrt{2\pi}\sigma}\right)\right) \qquad (7)$$

262 where erf is the error function. MAF is the asymptote of the measured SPAR curve at large particle
263 sizes. D_a is the midpoint activation diameter and is associated with the hygroscopicity of CCNs. σ is
264 the standard deviation of the cumulative Gaussian distribution function and indicates the heterogeneity
265 of CCN hygroscopicity. As reported by Jiang et al. (2021), based on the investigation of the

266 covariations between SPAR curves and parameterized hygroscopicity distribution, it was found that

267 the MAF can be used to estimate the number fraction of hygroscopic (thus CCN-active) particles, for

268 aerosol hygroscopicity distributions generally observed in ambient atmosphere, and thus half MAF

269 can be used to represent the number fraction of CCNs to total particles at particle size around D_a.

270 Although the influence of particles whose κ is less than 0.1 on SPAR cannot be considered in this

271 parameterization scheme, significant deviation were only found under higher SSs (Tao et al., 2020)

272 and need not to be considered under the low SSs discussed in this study.

273   To be noted, the meaning of MAF can be different regard to the SS, and SPAR measurement

274 up to about 400 nm is needed for the MAF fitting for SPAR at SS of 0.05% to represent the particles

275 with κ value higher than 0.1. For SPAR at SS of 0.8%, MAF should be 1 at 400 nm diameter. However,

276 a MAF of 1 in this case can lead to overestimations of hygroscopic particle number fraction due to the

277 significant difference between SPAR curves and sigmodal fitting curves. In the former study on SPAR

278 fitting curves in the NCP, it was found that a fitting parameterization with the combination of two

279 sigmodal fitting curves was needed for SPAR fitting at SSs higher than 0.4% (Tao et al., 2020).

280 However, in this study, we investigate SA formation on accumulation mode particles and particle CCN

281 activity at SSs below 0.1%, under which condition non-hygroscopic particles smaller than 400 nm are

282 typically CCN-inactive. The MAF fitted in the particle size range below 400 nm was used to indicate

283 the variations of SPAR that was of the main focus here in this work. In addition, due to the very low

284 N_{CCN} in particle size ranges larger than 400 nm, the deviations of N_{CCN} due to the limited range of

285 measured particle size are also very small.

286

3. Results

3.1. Overview of the measurements

The timeseries of meteorological parameters, SPAR, N_{CCN} at SS of 0.05% and mass concentration of Non-refractory particulate matter of $PM_{2.5}$ (NR-$PM_{2.5}$), $PM_{2.5}$ SA (inorganic compounds and OOA) and $PM_{2.5}$ PA (primary aerosol, defined as the sum of POA) are shown in Fig. 1. The mass concentration of OOA and four POA were quantified by the ACSM PMF analysis (Zhang et al. 2011). During the campaign, $PM_{2.5}$ PA were generally lower than 100 μg m^{-3} under both high and low RH periods. Meanwhile, $PM_{2.5}$ SA can approach about 400 μg m^{-3}, especially during the strong SA formation events under high RH conditions, but can be lower than 100 μg m^{-3} under low RH conditions. Strong diurnal variations were found in SPAR with varying meteorological parameters. During the whole period, the wind speed was generally lower than 4 m s^{-1}, which is in favor of aerosol particle accumulation and SA formation on existing particles. However, RH, N_{CCN}(0.05%), $PM_{2.5}$ SA and NR-$PM_{2.5}$ mass concentrations revealed very distinct levels before and after 4th Dec, and thus the whole campaign was divided into two stages with different RH and SA pollution conditions: higher RH and stronger SA pollution before 4th Dec, and lower RH and lighter SA pollution after 4th Dec. In the following discussions, the high RH stage corresponds to days before 4th Dec with daily maximum and minimum RH higher than 75% and 50%, respectively. Two events that occurred during 25th Nov to 27th Nov (Event 1) and 30th Nov to 2nd Dec (Event 2), respectively, displayed especially high RH conditions with successive nighttime fogs (blue shaded areas). The low RH stage corresponds to the period after 4th Dec with daily maximum and minimum RH below 70% and 30%, which was represented by two events that occurred during 9th Dec to 11th Dec (Event 3) and 13th Dec to 15th Dec (Event 4), respectively. These events were selected based on the similarity of $PM_{2.5}$ concentration and evolution, while the time window was fixed to two days for the convenience of intercomparing. In addition, during these events, the wind speed was generally low, the RH followed a general diurnal variations and SA mass grew steadily and continuously. Thus the interference of the variations of air mass and short-term local emissions can be eliminated and the influence of SA formation can be highlighted. It should be noted that variations of N_{CCN} at 0.07% were similar to those at 0.05%, which followed the variations of SA mass concentration. While at higher SSs, the variations of N_{CCN} differed from those of SA mass concentration, especially under high RH conditions, suggesting different responses of CCN activity towards distinct SA formation processes. As reported in Kuang et al. (2020c), during the high RH stage aqueous phase SA formation was promoted, leading to persistent increases in N_{CCN}(0.05% and 0.07%), mass concentration of NR-$PM_{2.5}$ and especially mass concentration of $PM_{2.5}$ SA during Event 1 and 2. During the low RH stage, the SA formation

320 dominantly occurred in the gas-phase, that generated much less SA than aqueous-phase formation

321 (Kuang et al., 2020c). Thus, the persistent increases of N_{CCN}(0.05% and 0.07%) and $PM_{2.5}$ during

322 Event 3 and 4 was much weaker than those in Events 1 and 2. Due to the different SA mass fractions,

323 SPAR during the high RH stage was generally higher than that during the low RH stage. However, the

324 ratios between N_{CCN}(0.05%) and mass concentration of $PM_{2.5}$ SA or NR-$PM_{2.5}$, were lower during the

325 high RH period and demonstrated strong decreases, especially in Event 1 and 2. The response of CCN

326 activity and N_{CCN}(0.05%) to the different SA formation mechanisms will be discussed

327 comprehensively in the following parts.

328 3.2. The influence of different secondary aerosol formation on the diurnal variation of CCN
329 activity

330   The diurnal averages of PNSD, SPAR at SS of 0.05%, GF-PDF for 200 nm particle and mass

331 fraction of particle chemical compositions during high RH periods before 4th Dec, low RH periods

332 after 4th Dec and the four events are shown in Fig. 2, respectively. To be noted, the "high (or low) RH

333 events" is used to refer to the SA formation events under high (or low) RH conditions for convivence,

334 and it doesn't mean that RH caused variations of CCN behavior. As can be seen in Figs. 2 (1b) and

335 (2b), different variations of SPAR due to SA formations can be found during the periods with different

336 RH conditions. The average diurnal variations of these parameters for the entire high RH stage and

337 low RH stage as shown in Figs. 2 (1a-1d) and (2a-2d) revealed similar but more smoothed variations

338 as in the four selected events. The four events are discussed and intercompared in the following to

339 magnify the differences under distinct RH conditions. For accumulation mode particles, particle

340 number concentrations were higher during daytime in high RH events, while stronger diurnal

341 variations occurred in low RH events. Simultaneous daytime increases in particle SPAR in size range

342 from 200 nm to 400 nm, GF-PDF in GF range from 1.2 to 1.8 hygroscopicity and SA mass fraction

343 were found in all four events, suggesting that SA formation led to increasing hygroscopic particles

344 number concentration, which in turn enhanced particle CCN activity. This effect was more pronounced

345 in Events 1 and 2 than in Events 3 and 4. In Events 1 and 2, SPAR values were generally higher than

346 0.4 at 200 nm and reached the maximum of 1 during noontime at 300 nm. A hygroscopic mode with

347 GF>1.4 was be found throughout the day, which dominated aerosol hygroscopicity during daytime.

348 Mass fraction of SA were generally higher than 70% and reach a maximum of 80% at noon. While in

349 Events 3 and 4, SPAR at 200 nm was lower than 0.4 at night and the maximum SPAR at 300 nm was

350 lower than 0.9. A particle mode with GF<1.1 dominates particle hygroscopicity, and the mass fraction

351 of SA was lower than 60% and 30% at noon and at night, respectively. However, stronger daytime

352 increase of SA mass fraction and accordingly larger variation in SPAR was observed in Events 3 and
353 4 than in Events 1 and 2.

354   Besides SS of 0.05%, variations of SPAR at SSs of 0.07% and 0.2% are also shown in Figs.
355 S1 and S2 in the supplement. And as shown in Figs. S1 and S2, the variations of SPAR and N_{CCN}/PM
356 at SS of 0.07% are similar but lighter, compared with those at SS of 0.05%. While for SS of 0.2%, the
357 difference of SPAR between different periods or events are smaller (Fig. S1), and so did the diurnal
358 variations of SPAR and GF-PDF at particle size of 100 nm (Fig. S2). Because CCN activity at SS of
359 0.2% was strong enough (indicated by SPAR value close to 1) in particle size range where the SA
360 formation dominates, and thus the different SA formations under high or low RH conditions cannot
361 lead to significant variations of CCN activity at SS of 0.2%. In summary, based on CCN measurements
362 in this study, the RH-dependent influence of SA formation on CCN activity can be found obviously at
363 SSs of 0.05% and 0.07%. As the variations of SPAR at SS of 0.07% were quite similar to those at SS
364 of 0.05%, further analysis was only based on CCN activity at SS of 0.05%.

365   In Fig. 3a, detailed comparison of particle CCN activity during SA formation events of N_{CCN}
366 enhancements at SS of 0.05% under different RH conditions are shown as the variations of SPAR
367 curves. Particle CCN activity in Events 1 and 2 were combined due to their similar diurnal variations
368 (as shown in Fig. 2). Besides SPAR curves (Fig. 3a), corresponding fitting parameters of the SPAR
369 curve including D_a and MAF were also shown in Figs. 3b and c, respectively, as enhanced SPAR for
370 particle population can be attributed to hygroscopic particle number fraction increase (MAF increase)
371 or enhancement of hygroscopic particle hygroscopicity (D_a decrease). Same as demonstrated in Fig. 2,
372 SPAR was generally higher and thus particle CCN activity(0.05%) were generally stronger in high RH
373 events than those in low RH events. However, as shown in Fig. 3a, the difference between SPAR in
374 high and low RH events at 300 nm decreased from 0.2 to 0.1 during the SA formations, indicating for
375 a stronger enhancement in low RH events, probably due to both the stronger increase of SA mass
376 fraction and the higher nighttime PA mass fraction (Fig. 2(e)). Furthermore, in high RH events, there
377 were daytime enhancements of SPAR within the 150 to 300 nm size range, as was indicated by the
378 daytime increase of MAF and decrease of Da, which mainly resulted from number fraction and
379 hygroscopicity increases of CCN-active particles. While in low RH events, the daytime enhancement
380 of SPAR was only observed for particles larger than 200 nm. This can be attributed to the strong
381 increase of MAF and the slight decrease of D_a, which indicates significant increasing number fraction
382 yet slightly enhanced hygroscopicity of hygroscopic particles, respectively. Overall, the enhancement
383 of SPAR was weaker but occurred at a broader particle size range in high RH events than in low RH
384 events, as shown in Fig. 3a. This is in accordance with previous the results from Kuang et al. (2020c),

suggesting that SA formation occurred mainly in aqueous phase within a broad particle size range (up to 1 μm) in high RH events, while SA formation dominantly proceeded via gas phase reactions and contributed to aerosol sizes smaller than 300 nm in low RH events. At SS of 0.05% (Fig. 3(a)), the variation of SPAR from 8:00-12:00 to 12:00-16:00 in particle size smaller than 200 nm was very small during low RH events, suggesting a smaller CCN activity enhancement due to SA formation compared with those at high RH events. In detail, the different variations of SPAR in high and low RH events indicated by MAF and D_a shown in Figs. 3(b & c) suggested different variations of hygroscopicity, number fraction and size of SA particles. Before SA formation, there was a significant difference between the MAF in high and low RH events, which disappeared after the SA formation. The stronger variations in MAF in low RH events suggested stronger enhancement of number concentration of formed SA particles. As for D_a during SA formation, there were similar, little decrease in both high and low RH events, suggesting similar hygroscopicity of the SA formed under low and high RH conditions. Thus differences of SPAR and the resultant N_{CCN} during low and high RH events were mainly due to the different variations of number fraction of formed SA particles.

As there were different influences of SA formation on both CCN activity at SS of 0.05% and PNSD under different RH conditions, different variation of N_{CCN}(0.05%) due to SA formation can also be expected. Fig. 4 displays the diurnal variation of $PM_{2.5}$ mass concentration, volume concentration (Vconc) , number concentration (Nconc) and N_{CCN}(0.05%) (all divided by CO to partially compensate for changes in planetary boundary layer height), as well as the N_{CCN}/$PM_{2.5}$ mass concentration ratio and SPAR during high and low RH events, respectively. Variables in Fig. 4 were also presented in Fig. S3 averaged for the entire high RH and low RH stages, respectively. Compared with the selected case events featuring significant N_{CCN} enhancement (Fig. 4(1c-2c)), the diurnal variations averaged for the entire high and low RH stages were similar, with higher levels of particle mass concentration but weaker enhancement of SA and N_{CCN}, indicating similar but weakened impact of SA formation on CCN activity due to the interference of other aerosol processes. Hereinafter, we discuss the variations in the four events to magnify the discrepancies of SA formation under high RH and low RH conditions and its distinct impact on N_{CCN}. The Vconc size distribution variations can be used as a proxy for the evolution of NR-$PM_{2.5}$ size distributions, considering the relatively small variations in particle density (ranging from 1.2 to 1.8 and with relative variations within 20% (Hu et al., 2012; Zhao et al., 2019)). The variations of the ratio between N_{CCN} (in different particle size range) and the mass concentration of $PM_{2.5}$ SA (referred as to N_{CCN}/SA) or NR-$PM_{2.5}$ (referred as to N_{CCN}/NR) can be used to evaluate the response of N_{CCN} to SA formation.

During high RH events, normalized N_{CCN}(0.05%) increased by ~ 50% from 8:00 to 14:00, with a similar increase in normalized $PM_{2.5}$ SA mass concentration (Fig. 4(1a)). As the $PM_{2.5}$ PA mass concentration decrease was much smaller than the SA increase, the NR-$PM_{2.5}$ mass concentration increase can be expected to be similar to the SA increase. As reported by Kuang et al. (2020c), SA during daytime were mainly formed at larger particle sizes, featuring Vconc increase in the particle size range of 400 to 1000 nm. In Fig. 4(1d), significant increases of particle number concentration (Nconc) in particle size range of 150 nm to 1000 nm can be observed. At larger particle size the increase of Nconc led to stronger increase of Vconc, which is why there was simultaneous but much weaker increases of Vconc in particle size range of 150 to 300 nm compared with increases of those in particle size of larger than 300 nm (Fig. 4(1b)). This suggests that $PM_{2.5}$ SA mainly contributed to particle sizes of larger than 300 nm. In addition, because the SA formation enhanced hygroscopicity and number fraction of CCN-active particles in particle size range of 150 to 300 nm, simultaneous enhancements of SPAR can be found throughout the measured particle size range of 180 to 300 nm (Fig. 4(1e)). By combining the enhancements of Nconc and SPAR in measured particle size ranges, there were increases of N_{CCN} from 200 to 500 nm (Fig. 4(1c)). ~~While the strongest Vconc increases occurred at particle sizes larger than 300 nm, the N_{CCN} increased most in the particle size range of 200 to 300 nm, suggesting that particles larger than 300 nm were already CCN-active before SA formation.~~ Thus while SA formation processes contributed to their volume (mass) and hygroscopicity increase, it had no further impact on N_{CCN}. As a result, N_{CCN} (>300 nm)/SA, N_{CCN} (<300 nm)/SA, N_{CCN} (>300 nm)/NR and N_{CCN} (<300 nm)/NR all decreased during the SA formation (Fig. 4(1f)), suggesting that weakening enhancement of N_{CCN}(0.05%) in SA formation under high RH condition as SA formation mainly added mass to already CCN-active particles .

During low RH events, weaker increases of both N_{CCN}(0.05%) and $PM_{2.5}$ SA mass concentration from 8:00 to 14:00 was found (Fig. 4(2a)). At the same time, PA mass decreased by 50% and the variation of total NR mass was small. Under low RH conditions, SA formation mainly contributed to mass enhancements of smaller particle sizes (Kuang et al., 2020c). Vconc increased mostly in the range of 150 to 300 nm (Fig. 4(2b)), while Nconc only increased within 300 nm (Fig. 4(2d)), suggesting that $PM_{2.5}$ SA mainly formed in particle size range ~~within~~ below 300 nm. SA formation mainly enhanced number fraction of CCN-active particles in particle size of 200 to 300 nm, as SPAR only revealed evident enhancement (Fig. 4(2e)) and N_{CCN} only significantly increased (Fig. 4(2c)) in that size range. As a result, although N_{CCN} (>300 nm)/SA decreased similar as that under high RH conditions, N_{CCN} (<300 nm)/SA and N_{CCN} (>300 nm)/NR generally stayed constant and N_{CCN} (<300 nm)/NR even increased during SA formation in daytime (Fig. 4(2f)). The ratio between bulk

450 N_{CCN} and mass concentration of NR-PM$_{2.5}$ became larger due to the SA formation, suggesting that

451 stronger enhancement of N_{CCN}(0.05%) in SA formation under low RH condition, because SA

452 formation mainly added mass to CCN-inactive particles and turned them into CCN-active particles.

453   In summary, during the campaign in this study, two kinds of SA formation events were

454 observed under different RH conditions with different variations of PM and N_{CCN} at SSs lower than

455 0.07%. Under high RH conditions, there were strong SIA dominated SA formation leading to stronger

456 enhancements of CCN-active particle number fraction ~~higher particle hygroscopicity~~ and N_{CCN}

457 ~~enhancements~~. Meanwhile, under low RH conditions, there were moderate SOA dominated SA

458 formation with moderate enhancements of CCN-active particle number fraction ~~particle~~

459 ~~hygroscopicity~~ and N_{CCN} ~~enhancements~~. However, for a unit amount of SA formation, the increase of

460 N_{CCN} was stronger under low RH conditions and weaker under high RH conditions. This was because

461 SA formation under low RH conditions was more concentrated on particle sizes smaller than 300 nm

462 and added more mass to CCN-inactive particles, turning them into CCN-active particles. In addition,

463 strong and distinct diurnal variations of CCN activity of particles were observed during different SA

464 formation processes, whose effects on N_{CCN} calculation need to be further evaluated.

465

466 **3.3. The influence of diurnal variation of CCN activity on N_{CCN} prediction**

467   Since PNSD measurements are generally ~~more~~ simpler and more common than N_{CCN}

468 measurements, N_{CCN} is usually estimated from real-time PNSD combined with parameterized CCN

469 activity. In former sections, it was already manifested that SA formations under different RH

470 conditions led to distinct variations in PNSD and SPAR at SS of 0.05%, ~~thus~~ hence different variations

471 in N_{CCN}. Thus, it is important for the prediction of N_{CCN} to quantify its sensitivity towards changes in

472 PNSD and SPAR during SA formation processes under different RH conditions.

473   In this study, ~~PNSD dominated the~~ N_{CCN} ~~calculation~~ was mostly determined by PNSD, as was

474 generally ~~found~~ the case in former studies (Dusek et al., 2006~~),~~). Suring SA formation events, ~~but~~

475 however, the variation of CCN activity also contributed significantly to the deviation of N_{CCN}

476 calculation ~~during SA formation~~. In former discussions, CCN activity (indicated by SPAR) at

477 0.05~~%~~ % SS revealed significant diurnal variations during this campaign, which were different during

478 SA formations under distinct RH conditions. The ratio ~~between~~ of N_{CCN} calculated based on campaign

479 averaged SPAR (N_{CCN_cal}) to those measured ~~N_{CCN} (N_{CCN_meas})~~ at 0.05% SS (N_{CCN_meas}) before and

480 after 4th Dec are shown in Fig. 5. SPAR is determined by the variation of D_a and MAF, which reflect

481 changes in hygroscopicity and number fraction of hygroscopic particles. Thus, to investigate the

482 ~~separate~~ respective influences of MAF and D_a variations on N_{CCN} predictions, N_{CCN_AvgMAF} (or

483 N_{CCN_avgDa}) was calculated based on the real-time PNSD and SPAR estimated by replacing MAF (or

484 D_a) in Eq. 7 with the campaign averaged value. During the high RH stage, underestimation of daytime

485 N_{CCN_cal} can reach up to 20%, since SPAR variations due to CCN activity enhancement were not

486 considered. Similar deviations of both N_{CCN_AvgMAF} and N_{CCN_avgDa} from N_{CCN_meas} were detected,

487 suggesting that both MAF and D_a variations contributed to N_{CCN_cal} underestimation under high RH

488 conditions. During the low RH stage, up to 50% overestimation existed in $N_{CCN\_AvgSPAR}$ ~~beyond~~ outside

489 SA formation ~~episodes~~ time periods. Only N_{CCN_AvgMAF} displayed similar deviations from N_{CCN_meas} as

490 $N_{CCN\_AvgSPAR}$, indicating that differences between N_{CCN_cal} and N_{CCN_meas} were mainly contributed by

491 variations in MAF brought on by significant CCN-active particles number fraction growth due to SA

492 formations. To be noted, $N_{CCN\_AvgSPAR}$ before and after 4th Dec ~~are~~ were both calculated ~~on the basis~~

493 based ~~of~~ on the ~~averaged~~ SPAR averaged ~~of~~ over ~~this~~ the entire campaign (green dots in Fig. 5a) ~~rather~~

494 ~~than the averaged SPAR before or after 4th~~, ~~because~~ since the applicability of ~~the~~ campaign averaged

495 SPAR ~~on~~ in ~~the~~ N_{CCN} calculation~~s in the NCP~~ was confirmed ~~in~~ by many former studies in the NCP

496 (Deng et al., 2012; Wang et al., 2013; Ma et al., 2016). During ~~the~~ low RH periods, SPAR ~~are~~ was

497 generally lower than the campaign averaged SPAR ~~of the campaign~~ and the ratio between the

498 calculated and measured N_{CCN} ~~are~~ were systematically higher (lasting for the whole night). In summary,

499 SA formation processes can induce significant deviation to N_{CCN} prediction that varied with RH

500 conditions, ~~which~~ and mainly resulted from the variation in~~of~~ MAF ~~and also varied under different~~

501 ~~RH conditions~~. Thus, for accurate N_{CCN} estimations, considering the variation of MAF (changes in the

502 fraction of the hygroscopic particles~~aerosol hygroscopicity~~) is highly essential.

503   As SOA is generally considered to be more hygroscopic than POA (Frosch et al., 2011; Lambe

504 et al., 2011; Kuang et al., 2020a), the increase of hygroscopic particles or SA particles (both SIA and

505 SOA) were considered to be the cause for the increase of SPAR within 200 to 300 nm size range (Fig.

506 2). In order to account for the variations of hygroscopic particles or SA particles in N_{CCN} calculation,

507 in the following part, Number Fraction of hygroscopic particles (GF(90%, 200 nm)>1.22, NF_{hygro})

508 measured by HTDMA and Mass Fraction of SA particles (MF_{SA}) measured by ACSM in this campaign

509 were used to represent MAF variations and to provide calculation of N_{CCN} at SS of 0.05% with smaller

510 deviations ~~combining~~ combined with PNSD measurement ~~with smaller deviations~~. To be noted, in

511 order to highlight the application of using MF_{SA} as estimation of MAF variations on N_{CCN} calculation,

512 the campaign averaged D_a from SPAR curves was used.

513   Based on the bulk hygroscopicity derived from particle chemical compositions measurements

514 (κ_{chem}), a critical diameter for CCN activation can be calculated based on κ-Köhler theory. ~~and based~~

515 ~~on~~ With this critical diameter, ~~which~~ N_{CCN}(0.05%) can be predicted ~~by~~ incorporating ~~combining~~

516 measured PNSD ~~with this critical diameter~~ (N_{CCN_Chem}). ~~Although there can be significant deviations~~

517 ~~for~~ κ of accumulation mode particles derived from chemical composition of the bulk aerosol might

518 bear significant uncertainties, which leads to significant deviations of N_{CCN} prediction. However, in

519 practice, ~~the measurements of~~ chemical compositions measurements specifically for~~of~~ accumulation

520 mode particles are not common, ~~and~~ thus bulk aerosol chemical composition~~s~~ ~~of the bulk aerosol is~~are

521 ~~still~~ commonly applied in CCN studies as substitute (Zhang et al., 2014; Zhang et al., 2016; Che et al.,

522 2017; Cai et al., 2018), especially when particle hygroscopicity measurements were in lack. As can be

523 seen ~~In~~ in Fig. 6(a), ~~it can be~~is ~~found that~~ N_{CCN_meas} at 0.05% SS was~~can be~~ strongly underestimated

524 by N_{CCN_Chem}, especially at lower N_{CCN_meas} ($\sim10^2$ # cm^{-3}), which is similar to the results of studies

525 that encountered high fractions of organics (Chang et al., 2010; Kawana et al., 2015). This deviation

526 between N_{CCN_meas} and N_{CCN_Chem} may have resulted from the hypothesis of internal mixing state and

527 the difference of particle hygroscopicity derived by particle chemical composition measurements and

528 CCN activity. Fig. 6(b) depicts the correlation between mass fraction of SA (MF$_{SA}$) and MAF at 0.05%

529 SS. MF$_{SA}$ was generally positively correlated to MAF (r=0.8) with slight underestimations, suggesting

530 that externally mixed SA dominated CCN-active particles. Thus, in the prediction of N_{CCN}, real-time

531 SPAR can be calculated from campaign average D_a and MAF assumed to be equal to real-time MF$_{SA}$

532 (N_{CCN_MF}). As displayed in Fig. 6(c), the underestimation and correlation between N_{CCN_cal} and

533 N_{CCN_meas} was improved after introducing MF$_{SA}$ into N_{CCN} calculation. Additionally, the diurnal

534 variations of N_{CCN_cal}/N_{CCN_meas} ratio based on different methods of N_{CCN} calculation during the whole

535 campaign were shown in Fig. 6(d). ~~It can be found that b~~By considering ~~the~~ real-time MF$_{SA}$ variations,

536 the deviation of calculated N_{CCN} (Real-time MF) can be reduced throughout the day, compared ~~with~~

537 to N_{CCN_Chem} (Real-time Chem). Meanwhile, ~~if~~using an averaged MF$_{SA}$ ~~is used~~ to estimate SPAR and

538 N_{CCN} could also reduce~~, the~~ deviations of calculated N_{CCN} (Averaged MF)~~can be reduced as well~~, ~~but~~

539 however, demonstrated a much stronger diurnal variation~~s~~ than the deviation of N_{CCN_MF}.

540 Based on the bulk hygroscopicity derived from GF measurement~~s~~ (κ_{GF}) at 200 nm, ~~a critical~~

541 ~~diameter~~D_a can be calculated based on the κ-Köhler theory, which can be applied to predict ~~and~~ N_{CCN}

542 at 0.05% SS (N_{CCN_GF})~~can be predicted by~~in ~~combining~~ combination with measured PNSD~~and the~~

543 ~~critical diameter (N_{CCN_GF})~~. Fig. 7(a) ~~shows~~reveals that N_{CCN_meas} were strongly underestimated by

544 N_{CCN_GF} (by more than 30~~%)~~. %), which~~This deviation~~ ~~may~~mightalso have result~~ed~~ from the

545 hypothesis of internal mixing state and the difference of particle hygroscopicity derived by GF and

546 particle CCN activity measured under different water vapor saturated conditions. Fig. 7(b) depicts the

547 positive correlation between NF$_{hygro}$ and MAF at 0.05% SS, which was weaker than that between MF$_{SA}$

548 and MAF. Similar as before, NF_{hygro} was applied as a proxy for MAF in the N_{CCN} calculation, which

549 also improved the underestimation and correlation between N_{CCN_cal} and N_{CCN_meas} (Fig. 7(c)). Also,

550 the campaign averaged D_a in Fig. 5a.was used to calculate SPAR curves and N_{CCN}. The diurnal

551 variations of the N_{CCN_cal}/N_{CCN_meas} ratio based on different methods of N_{CCN} calculation during the

552 whole campaign were are shown in Fig. 7(d). It can be found that bBy considering the real-time

553 variation of NF_{hygro}, the deviation of N_{CCN_NF} (Real-time NF) can wasbe reduced mainly reduced

554 during nighttime, compared with to N_{CCN_GF} (Real-time GF). Meanwhile, if applying an averaged

555 NF_{hygro} is used to estimate SPAR and N_{CCN}, reduced the deviations of calculated N_{CCN} (Averaged NF)

556 can be reduced during nighttime as well, but its deviations demonstrated a stronger diurnal variations

557 than the deviation of those of N_{CCN_NF}. If GF-PDF were directly used to calculate N_{CCN}, N_{CCN_cal} would

558 agree well with measured N_{CCN} (Fig. S4), because in this way the mixing state of aerosol would have

559 been accounted for. However, compared to the approach using GF-PDF, NF_{hygro} is easier to apply in

560 N_{CCN} calculation and can yield similar accuracies.

561 In summary, MAF exhibited strong diurnal variation that varied under different RH conditions

562 due to different SA formation mechanisms, which contributed most to N_{CCN} estimation deviations if

563 unaccounted for. The diurnal variations of MAF at the five measured SSs (Fig. S5) revealed significant

564 diurnal variations in MAF at low SSs (0.05% and 0.07%) that weare dependent on RH conditions,

565 while only small diurnal variations that weare insensitive to the RH conditions were detected at SSs

566 over above 0.2%. In general, MAF become became lower at lower SSs, especially during nighttime.

567 As the fraction of CCN-active particles were generally hygroscopic and composed of secondary

568 compounds, positive correlation was found between MAF, MF_{SA} and NF_{hygro}. Although a good

569 prediction of N_{CCN}(0.05%) was achieved by applying an averaged MAF (Figs. 5, 6d and 7d), in practice,

570 this would still require CCN measurements or HTDMA/chemical composition measurements as

571 proxies. Additionally, deviations of N_{CCN_cal} based on the averaged MAF can be large under low RH

572 conditions (Fig. 5c), while time-dependent MAF can eliminate a great part of these deviations. Thus,

573 by replacing MAF with real-time MF_{SA} or NF_{hygro} when deriving SPAR curves, the relative deviation

574 of N_{CCN}(0.05%) calculation can be reduced. The proposed N_{CCN} parameterization using MF_{SA} can also

575 be easily adopted by chemical-transport and climate models, improving their representation of N_{CCN}

576 changes due to distinct SA formation processes.

577

4. Conclusions

SA formation drives the development of haze pollution in the NCP and can result in significant variations of PNSD and aerosol hygroscopicity. Studies in the NCP have shown that the mechanism of SA formation can be affected by relative humidity (RH), and thus has different influences on the aerosol hygroscopicity and PNSD under distinct RH conditions. The difference in particle size where SA formation is taking place and the different chemical compositions of formed SA can result in different variations of CCN activity. Thus, it is essential to study the influence of SA formation on CCN activity of existing accumulation mode particles under different RH conditions in the NCP. As N_{CCN} is often predicted based on real-time PNSD and parameterized SPAR, the influence of varying SPAR in distinct SA formation processes on N_{CCN} calculation needs to be evaluated in detail.

Based on the measurements of CCN-activity, particle hygroscopicity, particle chemical composition, PNSD during the McFAN campaign in Gucheng winter 2018, the influences of SA formation on CCN activity and N_{CCN} calculation under different RH conditions were investigated especially at SSs lower than 0.07%. Two kinds of SA formation events were identified under different RH conditions with distinct variations in PM and N_{CCN} at 0.05% SS. Under high RH conditions, which corresponds to the periods with minimum RH higher than 50% in daytime, strong SA formation and $N_{CCN}(0.05\%)$ enhancements with strong hygroscopic particles and SIA dominated contribution to SA (>70%) was found. While under low RH conditions, which corresponds to the periods with daytime minimum RH below 30%, moderate SA formation and $N_{CCN}(0.05\%)$ enhancements with moderately hygroscopic particles and SOA dominated contribution to SA was found. However, the increase of N_{CCN} under the a same amount of SA formation was stronger under low RH conditions and weaker under high RH conditions. This was because the formation of SA under low RH conditions was more concentrated in particle size range smaller than 300 nm and added more mass to CCN-inactive particles turning them into CCN-active ones after SA formation.

In addition, strong diurnal variations of CCN activity of particles at 0.05% SS due to the strong SA formations were also observed, both varying with RH conditions. $N_{CCN}(0.05\%)$ was significantly underestimated when MAF (SPAR parameter) variations were not considered. As the fraction of CCN-active particles were generally hygroscopic and composed of secondary compounds, there were good correlation among MAF inferred from measurements of CCN activity, particle hygroscopicity and particle chemical compositions. Thus, the relative deviation of $N_{CCN}(0.05\%)$ estimation can be reduced by applying measurements of particle hygroscopicity or particle chemical compositions as a proxy for aerosol mixing state.

This study can further the understanding of the impact of SA formation on CCN activity and N_{CCN} calculation, specifically for SA formations on existing particles, which can strongly affect cloud microphysics properties in stratus clouds and fogs. The investigation of the influence of SA formation on CCN activity of existing particles in this study is important for improving N_{CCN} parameterizations in chemical-transport and climate models, so that they can account for the large variations induced by SA formation processes.

Supporting Information

The supporting information is available in a separate file.

Data availability.

The data used in this study are available from the corresponding author upon request (taojch@jnu.edu.cn and nan.ma@ jnu.edu.cn)

Author contributions.

JT, YK and NM designed this research. JT performed the data analysis and wrote the manuscript. YC, HS, NM, YK, JT, and JH planned this campaign. JT and YZ conducted the CCN measurements. YS and YH conducted the ACSM measurements and the ACSM PMF analysis. JH and QL conducted the HTDMA measurements. LX and YZ conducted the particle number size distribution measurements. WX conducted the measurements of CO and meteorological parameters. YC, HS, YS, YK and NM contributed to the revisions of this manuscript and all other coauthors have contributed to this paper in different ways.

Acknowledgement

We acknowledge the National Key Research and Development Program of China (grant no. 2017YFC0210104), the National Natural Science Foundation of China (grant no. 91644218 and 41805110), the Guangdong Innovative and Entrepreneurial Research Team Program (Research team on atmospheric environmental roles and effects of carbonaceous species: 2016ZT06N263), Special Fund Project for Science and Technology Innovation Strategy of Guangdong Province (2019B121205004) and the Basic Research Fund of CAMS (2020Z002)..

Conflicts of interest

638   There are no conflicts to declare.

639

640

Reference:

Cai, M., Tan, H., Chan, C. K., Qin, Y., Xu, H., Li, F., Schurman, M. I., Liu, L., and Zhao, J.: The size-resolved cloud condensation nuclei (CCN) activity and its prediction based on aerosol hygroscopicity and composition in the Pearl Delta River (PRD) region during wintertime 2014, Atmos. Chem. Phys., 18, 16419–16437, https://doi.org/10.5194/acp-18-16419-2018, 2018.

Chang, R. Y.-W., Slowik, J. G., Shantz, N. C., Vlasenko, A., Liggio, J., Sjostedt, S. J., Leaitch, W. R., and Abbatt, J. P. D.: The hygroscopicity parameter (κ) of ambient organic aerosol at a field site subject to biogenic and anthropogenic influences: relationship to degree of aerosol oxidation, Atmos. Chem. Phys., 10, 5047–5064, https://doi.org/10.5194/acp-10-5047-2010, 2010.

Che, H., Zhang, X., Zhang, L., Wang, Y., Zhang, Y., Shen, X., Ma, Q., Sun, J., and Zhong, J.: Prediction of size-resolved number concentration of cloud condensation nuclei and long-term measurements of their activation characteristics, Scientific reports, 7, 1–12, 2017.

Cheng, Y. F., Su, H., Rose, D., Gunthe, S. S., Berghof, M., Wehner, B., Achtert, P., Nowak, A., Takegawa, N., Kondo, Y., Shiraiwa, M., Gong, Y. G., Shao, M., Hu, M., Zhu, T., Zhang, Y. H., Carmichael, G. R., Wiedensohler, A., Andreae, M. O., and Pöschl, U.: Size-resolved measurement of the mixing state of soot in the megacity Beijing, China: diurnal cycle, aging and parameterization, Atmos. Chem. Phys., 12, 4477–4491, https://doi.org/10.5194/acp-12-4477-2012, 2012.

Dal Maso, M., Kulmala, M., Riipinen, I., Wagner, R., Hussein, T., Aalto, P. P., and Lehtinen, K. E. J.: Formation and growth of fresh atmospheric aerosols: eight years of aerosol size distribution data from SMEAR II, Hyytiala, Finland, 10, 323–336, 2005.

Deng, Z. Z., Zhao, C. S., Ma, N., Liu, P. F., Ran, L., Xu, W. Y., Chen, J., Liang, Z., Liang, S., Huang, M. Y., Ma, X. C., Zhang, Q., Quan, J. N., Yan, P., Henning, S., Mildenberger, K., Sommerhage, E., Schäfer, M., Stratmann, F., and Wiedensohler, A.: Size-resolved and bulk activation properties of aerosols in the North China Plain, Atmos. Chem. Phys., 11, 3835–3846, https://doi.org/10.5194/acp-11-3835-2011, 2011.

Deng, Z. Z., Zhao, C. S., Ma, N., Ran, L., Zhou, G. Q., Lu, D. R., and Zhou, X. J.: An examination of parameterizations for the CCN number concentration based on in situ measurements of aerosol activation properties in the North China Plain, Atmos. Chem. Phys., 13, 6227–6237, https://doi.org/10.5194/acp-13-6227-2013, 2013.

Ditas, F., Shaw, R. A., Siebert, H., Simmel, M., Wehner, B., and Wiedensohler, A.: Aerosols-cloud microphysics-thermodynamics-turbulence: evaluating supersaturation in a marine stratocumulus cloud, Atmos. Chem. Phys., 12, 2459–2468, https://doi.org/10.5194/acp-12-2459-2012, 2012.

Duan, J., Wang, Y., Xie, X., Li, M., Tao, J., Wu, Y., Cheng, T., Zhang, R., Liu, Y., Li, X., He, Q., Gao, W., and Wang, J.: Influence of pollutants on activity of aerosol cloud condensation nuclei (CCN) during pollution and post-rain periods in Guangzhou, southern China, 642, 1008–1019, https://doi.org/10.1016/j.scitotenv.2018.06.053, 2018.

Dusek, U., Frank, G., Hildebrandt, L., Curtius, J., Schneider, J., Walter, S., Chand, D., Drewnick, F., Hings, S., and Jung, D.: Size matters more than chemistry for cloud-nucleating ability of aerosol particles, Science, 312, 1375–1378, 2006.

Fan, J., Wang, Y., Rosenfeld, D., and Liu, X.: Review of Aerosol–Cloud Interactions: Mechanisms, Significance, and Challenges, Journal of the Atmospheric Sciences, 73, 4221–4252, https://doi.org/10.1175/JAS-D-16-0037.1, 2016.

Farmer, D. K., Cappa, C. D., and Kreidenweis, S. M.: Atmospheric Processes and Their Controlling Influence on Cloud Condensation Nuclei Activity, 115, 4199–4217, https://doi.org/10.1021/cr5006292, 2015.

Frosch, M., Bilde, M., DeCarlo, P., Jurányi, Z., Tritscher, T., Dommen, J., Donahue, N., Gysel, M., Weingartner, E., and Baltensperger, U.: Relating cloud condensation nuclei activity and oxidation level of α-pinene secondary organic aerosols, Journal of Geophysical Research: Atmospheres, 116, 2011.

Gordon, H., Sengupta, K., Rap, A., Duplissy, J., Frege, C., Williamson, C., Heinritzi, M., Simon, M., Yan, C., Almeida, J., Trostl, J., Nieminen, T., Ortega, I. K., Wagner, R., Dunne, E. M., Adamov, A., Amorim, A., Bernhammer, A.-K., Bianchi, F., Breitenlechner, M., Brilke, S., Chen, X., Craven, J. S., Dias, A., Ehrhart, S., Fischer, L., Flagan, R. C., Franchin, A., Fuchs, C., Guida, R., Hakala, J., Hoyle, C. R., Jokinen, T., Junninen, H., Kangasluoma, J., Kim, J., Kirkby, J., Krapf, M., Kuerten, A., Laaksonen, A., Lehtipalo, K., Makhmutov, V., Mathot, S., Molteni, U., Monks, S. A., Onnela, A., Perakyla, O., Piel, F., Petaja, T., Praplan, A. P., Pringle, K. J., Richards, N. A. D., Rissanen, M. P., Rondo, L., Sarnela, N., Schobesberger, S., Scott, C. E., Seinfeldo, J. H., Sharma, S., Sipila, M., Steiner, G., Stozhkov, Y., Stratmann, F., Tome, A., Virtanen, A., Vogel, A. L., Wagner, A. C., Wagner, P. E., Weingartner, E., Wimmer, D., Winkler, P. M., Ye, P., Zhang, X., Hansel, A., Dommen, J., Donahue, N. M., Worsnop, D. R., Baltensperger, U., Kulmala, M., Curtius, J., and Carslaw, K. S.: Reduced

701 anthropogenic aerosol radiative forcing caused by biogenic new particle formation, 113, 12053–12058,
702 https://doi.org/10.1073/pnas.1602360113, 2016.

703 Gryspeerdt, E. and Stier, P.: Regime-based analysis of aerosol-cloud interactions, Geophysical
704 Research Letters, 39, https://doi.org/10.1029/2012GL053221, 2012.

705 Gysel, M., Crosier, J., Topping, D. O., Whitehead, J. D., Bower, K. N., Cubison, M. J., Williams, P.
706 I., Flynn, M. J., McFiggans, G. B., and Coe, H.: Closure study between chemical composition and
707 hygroscopic growth of aerosol particles during TORCH2, Atmos. Chem. Phys., 7, 6131–6144,
708 https://doi.org/10.5194/acp-7-6131-2007, 2007.

709 Gysel, M., McFiggans, G. B., and Coe, H.: Inversion of tandem differential mobility analyser (TDMA)
710 measurements, 40, 134–151, https://doi.org/10.1016/j.jaerosci.2008.07.013, 2009.

711 Hagen, D. E. and Alofs, D. J.: Linear Inversion Method to Obtain Aerosol Size Distributions from
712 Measurements with a Differential Mobility Analyzer, Aerosol Science and Technology, 2, 465–475,
713 https://doi.org/10.1080/02786828308958650, 1983.

714 Hammer, E., Bukowiecki, N., Gysel, M., Jurányi, Z., Hoyle, C. R., Vogt, R., Baltensperger, U., and
715 Weingartner, E.: Investigation of the effective peak supersaturation for liquid-phase clouds at the high-
716 alpine site Jungfraujoch, Switzerland (3580 m a.s.l.), Atmos. Chem. Phys., 14, 1123–1139,
717 https://doi.org/10.5194/acp-14-1123-2014, 2014a.

718 Hammer, E., Gysel, M., Roberts, G. C., Elias, T., Hofer, J., Hoyle, C. R., Bukowiecki, N., Dupont, J.-
719 C., Burnet, F., Baltensperger, U., and Weingartner, E.: Size-dependent particle activation properties in
720 fog during the ParisFog 2012/13 field campaign, Atmos. Chem. Phys., 14, 10517–10533,
721 https://doi.org/10.5194/acp-14-10517-2014, 2014b.

722 Hong, J., Xu, H., Tan, H., Yin, C., and Kerminen, V. M.: Mixing state and particle hygroscopicity of
723 organic-dominated aerosols over the Pearl River Delta region in China, Atmos. Chem. Phys., 18,
724 14079–14094, 2018.

725 Hu, M., Peng, J., Sun, K., Yue, D., Guo, S., Wiedensohler, A., and Wu, Z.: Estimation of Size-
726 Resolved Ambient Particle Density Based on the Measurement of Aerosol Number, Mass, and
727 Chemical Size Distributions in the Winter in Beijing, Environ. Sci. Technol., 46, 9941–9947,
728 https://doi.org/10.1021/es204073t, 2012.

729 Hu, W., Hu, M., Hu, W., Jimenez, J. L., Yuan, B., Chen, W., Wang, M., Wu, Y., Chen, C., Wang, Z.,
730 Peng, J., Zeng, L., and Shao, M.: Chemical composition, sources, and aging process of submicron

aerosols in Beijing: Contrast between summer and winter, Journal of Geophysical Research: Atmospheres, 121, 1955–1977, https://doi.org/10.1002/2015JD024020, 2016.

Hu, W., Campuzano-Jost, P., Day, D. A., Croteau, P., Canagaratna, M. R., Jayne, J. T., Worsnop, D. R., and Jimenez, J. L.: Evaluation of the new capture vapourizer for aerosol mass spectrometers (AMS) through laboratory studies of inorganic species, Atmos. Meas. Tech., 10, 2897–2921, https://doi.org/10.5194/amt-10-2897-2017, 2017a.

Hu, W., Hu, M., Hu, W.-W., Zheng, J., Chen, C., Wu, Y., and Guo, S.: Seasonal variations in high time-resolved chemical compositions, sources, and evolution of atmospheric submicron aerosols in the megacity Beijing, Atmos. Chem. Phys., 17, 9979–10000, https://doi.org/10.5194/acp-17-9979-2017, 2017b.

Huang, R.-J., Zhang, Y., Bozzetti, C., Ho, K.-F., Cao, J.-J., Han, Y., Daellenbach, K. R., Slowik, J. G., Platt, S. M., Canonaco, F., Zotter, P., Wolf, R., Pieber, S. M., Bruns, E. A., Crippa, M., Ciarelli, G., Piazzalunga, A., Schwikowski, M., Abbaszade, G., Schnelle-Kreis, J., Zimmermann, R., An, Z., Szidat, S., Baltensperger, U., Haddad, I. E., and Prévôt, A. S. H.: High secondary aerosol contribution to particulate pollution during haze events in China, Nature, 514, 218–222, https://doi.org/10.1038/nature13774, 2014.

Jia, H., Ma, X., Yu, F., Liu, Y., and Yin, Y.: Distinct Impacts of Increased Aerosols on Cloud Droplet Number Concentration of Stratus/Stratocumulus and Cumulus, Geophysical Research Letters, n/a, https://doi.org/10.1029/2019GL085081, 2019.

Jiang, X., Tao, J., Kuang, Y., Hong, J., and Ma, N.: Mathematical derivation and physical interpretation of particle size-resolved activation ratio based on particle hygroscopicity distribution: Application on global characterization of CCN activity, Atmospheric Environment, 246, 118137, https://doi.org/10.1016/j.atmosenv.2020.118137, 2021.

Kawana, K., Nakayama, T., and Mochida, M.: Hygroscopicity and CCN activity of atmospheric aerosol particles and their relation to organics: Characteristics of urban aerosols in Nagoya, Japan, 121, 4100–4121, https://doi.org/10.1002/2015jd023213, 2016.

Kerminen, V.-M., Paramonov, M., Anttila, T., Riipinen, I., Fountoukis, C., Korhonen, H., Asmi, E., Laakso, L., Lihavainen, H., Swietlicki, E., Svenningsson, B., Asmi, A., Pandis, S. N., Kulmala, M., and Petaja, T.: Cloud condensation nuclei production associated with atmospheric nucleation: a synthesis based on existing literature and new results, 12, 12037–12059, https://doi.org/10.5194/acp-12-12037-2012, 2012.

Köhler, H.: The nucleus in and the growth of hygroscopic droplets, 32, 1152–1161, 1936.

Krüger, M. L., Mertes, S., Klimach, T., Cheng, Y. F., Su, H., Schneider, J., Andreae, M. O., Pöschl, U., and Rose, D.: Assessment of cloud supersaturation by size-resolved aerosol particle and cloud condensation nuclei (CCN) measurements, Atmos. Meas. Tech., 7, 2615–2629, https://doi.org/10.5194/amt-7-2615-2014, 2014.

Kuang, Y., Xu, W., Tao, J., Ma, N., Zhao, C., and Shao, M.: A Review on Laboratory Studies and Field Measurements of Atmospheric Organic Aerosol Hygroscopicity and Its Parameterization Based on Oxidation Levels, Current Pollution Reports, 1–15, 2020a.

Kuang, Y., He, Y., Xu, W., Zhao, P., Cheng, Y., Zhao, G., Tao, J., Ma, N., Su, H., Zhang, Y., Sun, J., Cheng, P., Yang, W., Zhang, S., Wu, C., Sun, Y., and Zhao, C.: Distinct diurnal variation in organic aerosol hygroscopicity and its relationship with oxygenated organic aerosol, Atmos. Chem. Phys., 20, 865–880, https://doi.org/10.5194/acp-20-865-2020, 2020b.

Kuang, Y., He, Y., Xu, W., Yuan, B., Zhang, G., Ma, Z., Wu, C., Wang, C., Wang, S., Zhang, S., Tao, J., Ma, N., Su, H., Cheng, Y., Shao, M., and Sun, Y.: Photochemical Aqueous-Phase Reactions Induce Rapid Daytime Formation of Oxygenated Organic Aerosol on the North China Plain, 54, 3849–3860, https://doi.org/10.1021/acs.est.9b06836, 2020c.

Kulmala, M., Riipinen, I., Sipila, M., Manninen, H. E., Petaja, T., Junninen, H., Dal Maso, M., Mordas, G., Mirme, A., Vana, M., Hirsikko, A., Laakso, L., Harrison, R. M., Hanson, I., Leung, C., Lehtinen, K. E. J., and Kerminen, V.-M.: Toward direct measurement of atmospheric nucleation, 318, 89–92, https://doi.org/10.1126/science.1144124, 2007.

Lambe, A. T., Onasch, T. B., Massoli, P., Croasdale, D. R., Wright, J. P., Ahern, A. T., Williams, L. R., Worsnop, D. R., Brune, W. H., and Davidovits, P.: Laboratory studies of the chemical composition and cloud condensation nuclei (CCN) activity of secondary organic aerosol (SOA) and oxidized primary organic aerosol (OPOA), 11, 8913–8928, https://doi.org/10.5194/acp-11-8913-2011, 2011.

Li, G., Su, H., Ma, N., Tao, J., Kuang, Y., Wang, Q., Hong, J., Zhang, Y., Kuhn, U., and Zhang, S.: Multiphase chemistry experiment in Fogs and Aerosols in the North China Plain (McFAN): integrated analysis and intensive winter campaign 2018, Faraday Discussions, 2021.

Liu, H. J., Zhao, C. S., Nekat, B., Ma, N., Wiedensohler, A., van Pinxteren, D., Spindler, G., Müller, K., and Herrmann, H.: Aerosol hygroscopicity derived from size-segregated chemical composition and its parameterization in the North China Plain, Atmos. Chem. Phys., 14, 2525–2539, https://doi.org/10.5194/acp-14-2525-2014, 2014.

793   Liu, P. F., Zhao, C. S., Göbel, T., Hallbauer, E., Nowak, A., Ran, L., Xu, W. Y., Deng, Z. Z., Ma, N.,

794   and Mildenberger, K.: Hygroscopic properties of aerosol particles at high relative humidity and their

795   diurnal variations in the North China Plain, 11, 3479–3494, 2011.

796   Liu, Z., Wang, Y., Gu, D., Zhao, C., Huey, L. G., Stickel, R., Liao, J., Shao, M., Zhu, T., Zeng, L.,

797   Liu, S.-C., Chang, C.-C., Amoroso, A., and Costabile, F.: Evidence of Reactive Aromatics As a Major

798   Source of Peroxy Acetyl Nitrate over China, Environ. Sci. Technol., 44, 7017–7022,

799   https://doi.org/10.1021/es1007966, 2010.

800   Ma, N., Zhao, C., Tao, J., Wu, Z., Kecorius, S., Wang, Z., Größ, J., Liu, H., Bian, Y., Kuang, Y., Teich,

801   M., Spindler, G., Müller, K., van Pinxteren, D., Herrmann, H., Hu, M., and Wiedensohler, A.:

802   Variation of CCN activity during new particle formation events in the North China Plain, Atmos.

803   Chem. Phys., 16, 8593–8607, https://doi.org/10.5194/acp-16-8593-2016, 2016.

804   Mei, F., Hayes, P. L., Ortega, A., Taylor, J. W., Allan, J. D., Gilman, J., Kuster, W., de Gouw, J.,

805   Jimenez, J. L., and Wang, J.: Droplet activation properties of organic aerosols observed at an urban

806   site during CalNex-LA, 118, 2903–2917, https://doi.org/10.1002/jgrd.50285, 2013.

807   Petters, M. D. and Kreidenweis, S. M.: A single parameter representation of hygroscopic growth and

808   cloud condensation nucleus activity, Atmos. Chem. Phys., 7, 1961–1971, 2007.

809   Reutter, P., Su, H., Trentmann, J., Simmel, M., Rose, D., Gunthe, S. S., Wernli, H., Andreae, M. O.,

810   and Pöschl, U.: Aerosol- and updraft-limited regimes of cloud droplet formation: influence of particle

811   number, size and hygroscopicity on the activation of cloud condensation nuclei (CCN), Atmos. Chem.

812   Phys., 9, 7067–7080, https://doi.org/10.5194/acp-9-7067-2009, 2009.

813   Roberts, G. C. and Nenes, A.: A continuous-flow streamwise thermal-gradient CCN chamber for

814   atmospheric measurements, 39, 206–221, 2005.

815   Rose, D., Gunthe, S. S., Mikhailov, E., Frank, G. P., Dusek, U., Andreae, M. O., and Pöschl, U.:

816   Calibration and measurement uncertainties of a continuous-flow cloud condensation nuclei counter

817   (DMT-CCNC): CCN activation of ammonium sulfate and sodium chloride aerosol particles in theory

818   and experiment, Atmos. Chem. Phys., 8, 1153–1179, 2008.

819   Rose, D., Nowak, A., Achtert, P., Wiedensohler, A., Hu, M., Shao, M., Zhang, Y., Andreae, M. O.,

820   and Poschl, U.: Cloud condensation nuclei in polluted air and biomass burning smoke near the mega-

821   city Guangzhou, China - Part 1: Size-resolved measurements and implications for the modeling of

822   aerosol particle hygroscopicity and CCN activity, Atmos. Chem. Phys., 10, 3365–3383, 2010.

823 Rose, D., Gunthe, S. S., Su, H., Garland, R. M., Yang, H., Berghof, M., Cheng, Y. F., Wehner, B.,
824 Achtert, P., Nowak, A., Wiedensohler, A., Takegawa, N., Kondo, Y., Hu, M., Zhang, Y., Andreae, M.
825 O., and Poschl, U.: Cloud condensation nuclei in polluted air and biomass burning smoke near the
826 mega-city Guangzhou, China -Part 2: Size-resolved aerosol chemical composition, diurnal cycles, and
827 externally mixed weakly CCN-active soot particles, Atmos. Chem. Phys., 11, 2817–2836,
828 https://doi.org/10.5194/acp-11-2817-2011, 2011.

829 Shen, C., Zhao, C., Ma, N., Tao, J., Zhao, G., Yu, Y., and Kuang, Y.: Method to Estimate Water Vapor
830 Supersaturation in the Ambient Activation Process Using Aerosol and Droplet Measurement Data,
831 Journal of Geophysical Research: Atmospheres, 123, 10,606-10,619,
832 https://doi.org/10.1029/2018JD028315, 2018.

833 Su, H., Rose, D., Cheng, Y. F., Gunthe, S. S., Massling, A., Stock, M., Wiedensohler, A., Andreae, M.
834 O., and Poschl, U.: Hygroscopicity distribution concept for measurement data analysis and modeling
835 of aerosol particle mixing state with regard to hygroscopic growth and CCN activation, Atmos. Chem.
836 Phys., 10, 7489–7503, https://doi.org/10.5194/acp-10-7489-2010, 2010.

837 Sun, Y., He, Y., Kuang, Y., Xu, W., Song, S., Ma, N., Tao, J., Cheng, P., Wu, C., Su, H., Cheng, Y.,
838 Xie, C., Chen, C., Lei, L., Qiu, Y., Fu, P., Croteau, P., and Worsnop, D. R.: Chemical Differences
839 Between PM1 and PM2.5 in Highly Polluted Environment and Implications in Air Pollution Studies,
840 47, e2019GL086288, https://doi.org/10.1029/2019GL086288, 2020.

841 Tan, H., Xu, H., Wan, Q., Li, F., Deng, X., Chan, P. W., Xia, D., and Yin, Y.: Design and Application
842 of an Unattended Multifunctional H-TDMA System, 30, 1136–1148, https://doi.org/10.1175/JTECH-
843 D-12-00129.1, 2013.

844 Tao, J., Kuang, Y., Ma, N., Zheng, Y., Wiedensohler, A., and Zhao, C.: An improved parameterization
845 scheme for size-resolved particle activation ratio and its application on comparison study of particle
846 hygroscopicity measurements between HTDMA and DMA-CCNC, 226, 117403,
847 https://doi.org/10.1016/j.atmosenv.2020.117403, 2020.

848 Thalman, R., de Sa, S. S., Palm, B. B., Barbosa, H. M. J., Poehlker, M. L., Alexander, M. L., Brito, J.,
849 Carbone, S., Castillo, P., Day, D. A., Kuang, C., Manzi, A., Ng, N. L., Sedlacek, A. J., Souza, R.,
850 Springston, S., Watson, T., Poehlker, C., Poeschl, U., Andreae, M. O., Artaxo, P., Jimenez, J. L.,
851 Martin, S. T., and Wang, J.: CCN activity and organic hygroscopicity of aerosols downwind of an
852 urban region in central Amazonia: seasonal and diel variations and impact of anthropogenic emissions,
853 17, 11779–11801, https://doi.org/10.5194/acp-17-11779-2017, 2017.

854 Wang, Y., Chen, J., Wang, Q., Qin, Q., Ye, J., Han, Y., Li, L., Zhen, W., Zhi, Q., Zhang, Y., and Cao,
855 J.: Increased secondary aerosol contribution and possible processing on polluted winter days in China,
856 Environment International, 127, 78–84, https://doi.org/10.1016/j.envint.2019.03.021, 2019.

857 Wang, Z., Cheng, Y., Ma, N., Mikhailov, E., Pöschl, U., and Su, H.: Dependence of the hygroscopicity
858 parameter κ on particle size, humidity and solute concentration: implications for laboratory
859 experiments, field measurements and model studies, Atmos. Chem. Phys. Discuss., 2017, 1–33,
860 https://doi.org/10.5194/acp-2017-253, 2017.

861 Wiedensohler, A., Cheng, Y. F., Nowak, A., Wehner, B., Achtert, P., Berghof, M., Birmili, W., Wu,
862 Z. J., Hu, M., Zhu, T., Takegawa, N., Kita, K., Kondo, Y., Lou, S. R., Hofzumahaus, A., Holland, F.,
863 Wahner, A., Gunthe, S. S., Rose, D., Su, H., and Poeschl, U.: Rapid aerosol particle growth and
864 increase of cloud condensation nucleus activity by secondary aerosol formation and condensation: A
865 case study for regional air pollution in northeastern China, 114, D00G08,
866 https://doi.org/10.1029/2008JD010884, 2009.

867 Williams, B. J., Goldstein, A. H., Kreisberg, N. M., Hering, S. V., Worsnop, D. R., Ulbrich, I. M.,
868 Docherty, K. S., and Jimenez, J. L.: Major components of atmospheric organic aerosol in southern
869 California as determined by hourly measurements of source marker compounds, Atmos. Chem. Phys.,
870 10, 11577–11603, https://doi.org/10.5194/acp-10-11577-2010, 2010.

871 Wu, Z. J., Poulain, L., Birmili, W., Groess, J., Niedermeier, N., Wang, Z. B., Herrmann, H., and
872 Wiedensohler, A.: Some insights into the condensing vapors driving new particle growth to CCN sizes
873 on the basis of hygroscopicity measurements, 15, 13071–13083, https://doi.org/10.5194/acp-15-
874 13071-2015, 2015.

875 Wu, Z. J., Zheng, J., Shang, D. J., Du, Z. F., Wu, Y. S., Zeng, L. M., Wiedensohler, A., and Hu, M.:
876 Particle hygroscopicity and its link to chemical composition in the urban atmosphere of Beijing, China,
877 during summertime, Atmos. Chem. Phys., 16, 1123–1138, https://doi.org/10.5194/acp-16-1123-2016,
878 2016.

879 Xu, W., Han, T., Du, W., Wang, Q., Chen, C., Zhao, J., Zhang, Y., Li, J., Fu, P., Wang, Z., Worsnop,
880 D. R., and Sun, Y.: Effects of Aqueous-Phase and Photochemical Processing on Secondary Organic
881 Aerosol Formation and Evolution in Beijing, China, Environ. Sci. Technol., 51, 762–770,
882 https://doi.org/10.1021/acs.est.6b04498, 2017a.

883 Xu, W., Croteau, P., Williams, L., Canagaratna, M., Onasch, T., Cross, E., Zhang, X., Robinson, W.,
884 Worsnop, D., and Jayne, J.: Laboratory characterization of an aerosol chemical speciation monitor

885 with PM2.5 measurement capability, Aerosol Science and Technology, 51, 69–83,
886 https://doi.org/10.1080/02786826.2016.1241859, 2017b.

887 Xu, W., Sun, Y., Wang, Q., Zhao, J., Wang, J., Ge, X., Xie, C., Zhou, W., Du, W., Li, J., Fu, P., Wang,
888 Z., Worsnop, D. R., and Coe, H.: Changes in Aerosol Chemistry From 2014 to 2016 in Winter in
889 Beijing: Insights From High-Resolution Aerosol Mass Spectrometry, Journal of Geophysical Research:
890 Atmospheres, 124, 1132–1147, https://doi.org/10.1029/2018JD029245, 2019.

891 Xu, W. Q., Sun, Y. L., Chen, C., Du, W., Han, T. T., Wang, Q. Q., Fu, P. Q., Wang, Z. F., Zhao, X. J.,
892 Zhou, L. B., Ji, D. S., Wang, P. C., and Worsnop, D. R.: Aerosol composition, oxidation properties,
893 and sources in Beijing: results from the 2014 Asia-Pacific Economic Cooperation summit study,
894 Atmos. Chem. Phys., 15, 13681–13698, https://doi.org/10.5194/acp-15-13681-2015, 2015.

895 Yu, F., Luo, G., Nair, A. A., Schwab, J. J., Sherman, J. P., and Zhang, Y.: Wintertime new particle
896 formation and its contribution to cloud condensation nuclei in the Northeastern United States, Atmos.
897 Chem. Phys., 20, 2591–2601, https://doi.org/10.5194/acp-20-2591-2020, 2020.

898 Yue, D., Zhong, L., Zhang, T., Shen, J., Yuan, L., Ye, S., Zhou, Y., and Zeng, L.: Particle Growth and
899 Variation of Cloud Condensation Nucleus Activity on Polluted Days with New Particle Formation: A
900 Case Study for Regional Air Pollution in the PRD Region, China, 16, 323–335,
901 https://doi.org/10.4209/aaqr.2015.06.0381, 2016.

902 Zhang, F., Li, Y., Li, Z., Sun, L., Li, R., Zhao, C., Wang, P., Sun, Y., Liu, X., Li, J., Li, P., Ren, G.,
903 and Fan, T.: Aerosol hygroscopicity and cloud condensation nuclei activity during the AC3Exp
904 campaign: implications for cloud condensation nuclei parameterization, Atmos. Chem. Phys., 14,
905 13423–13437, https://doi.org/10.5194/acp-14-13423-2014, 2014.

906 Zhang, F., Li, Z., Li, Y., Sun, Y., Wang, Z., Li, P., Sun, L., Wang, P., Cribb, M., Zhao, C., Fan, T.,
907 Yang, X., and Wang, Q.: Impacts of organic aerosols and its oxidation level on CCN activity from
908 measurement at a suburban site in China, 16, 5413–5425, https://doi.org/10.5194/acp-16-5413-2016,
909 2016.

910 Zhang, F., Ren, J., Fan, T., Chen, L., Xu, W., Sun, Y., Zhang, R., Liu, J., Jiang, S., Jin, X., Wu, H., Li,
911 S., Cribb, M. C., and Li, Z.: Significantly enhanced aerosol CCN activity and number concentrations
912 by nucleation-initiated haze events: a case study in urban Beijing, Journal of Geophysical Research:
913 Atmospheres, n/a, https://doi.org/10.1029/2019JD031457, 2019.

914 Zhang, Q., Jimenez, J. L., Canagaratna, M. R., Ulbrich, I. M., Ng, N. L., Worsnop, D. R., and Sun, Y.:
915 Understanding atmospheric organic aerosols via factor analysis of aerosol mass spectrometry: a review,

916 Analytical and Bioanalytical Chemistry, 401, 3045–3067, https://doi.org/10.1007/s00216-011-5355-

917 y, 2011.

918 Zhang, R., Khalizov, A., Wang, L., Hu, M., and Xu, W.: Nucleation and Growth of Nanoparticles in

919 the Atmosphere, 112, 1957–2011, https://doi.org/10.1021/cr2001756, 2012.

920 Zhao, G., Tan, T., Zhao, W., Guo, S., Tian, P., and Zhao, C.: A new parameterization scheme for the

921 real part of the ambient urban aerosol refractive index, 19, 12875–12885, https://doi.org/10.5194/acp-

922 19-12875-2019, 2019.

923

 Figures:
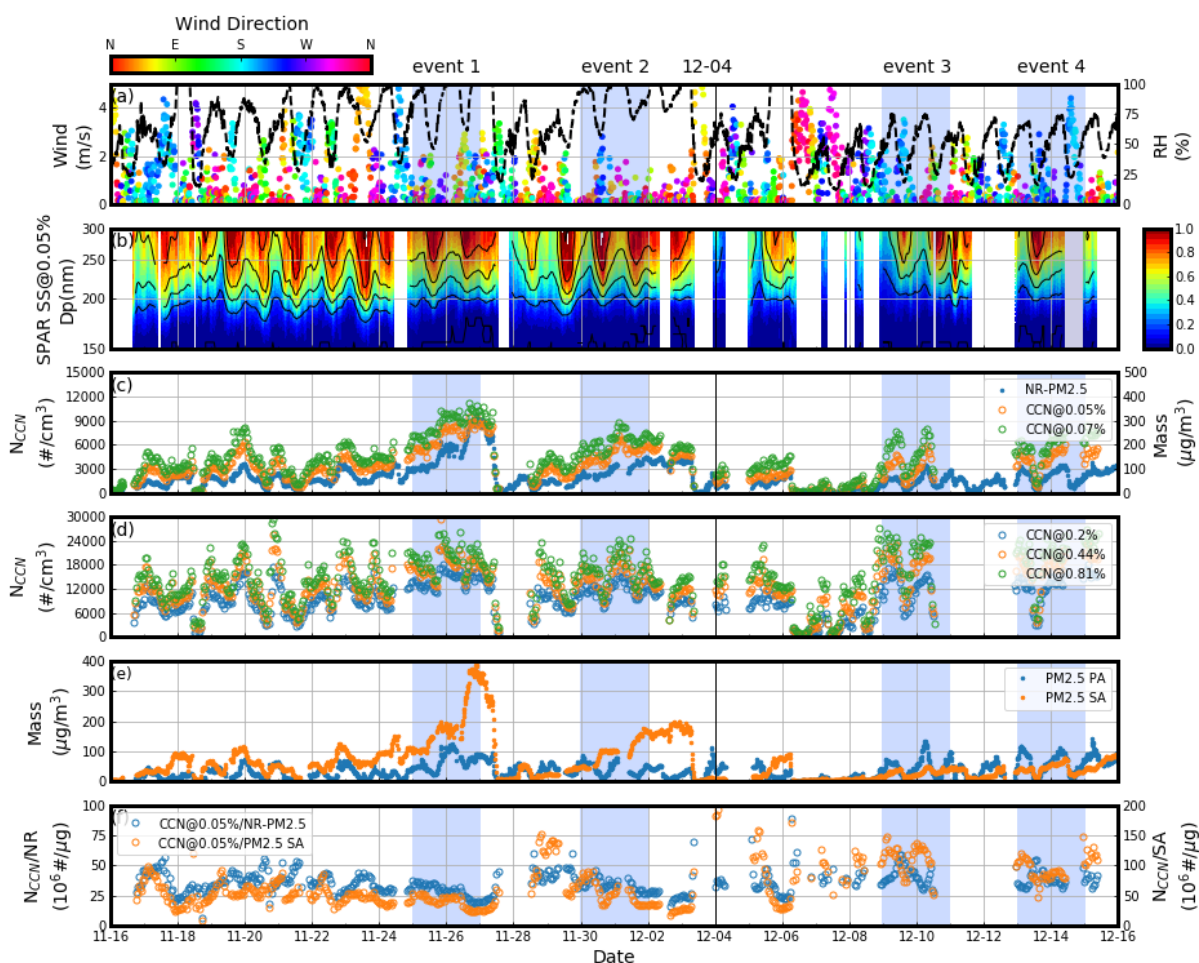
926 Fig 1. Overview of the measurements during the campaign: (a) dots represent wind speed with color

927 indicating wind direction, and black lines represent RH; (b) SPAR under SS of 0.05%; (c) blue, green

928 and yellow dots represent N_{CCN} under SS of 0.05% and 0.07%, and mass concentration of NR-PM2.5,

929 respectively; (d) blue, green and yellow dots represent N_{CCN} under SS of 0.2%, 0.44% and 0.81%,

930 respectively; (e) blue and yellow dots represent mass concentration of $PM_{2.5}$ PA and $PM_{2.5}$ SA

931 respectively; (f) blue and yellow dots represent ratio between N_{CCN} and mass concentration of NR-

932 $PM_{2.5}$ and $PM_{2.5}$ SA, respectively. There were four events with significant enhancements of N_{CCN}

933 during the blue shaded periods.

934

935
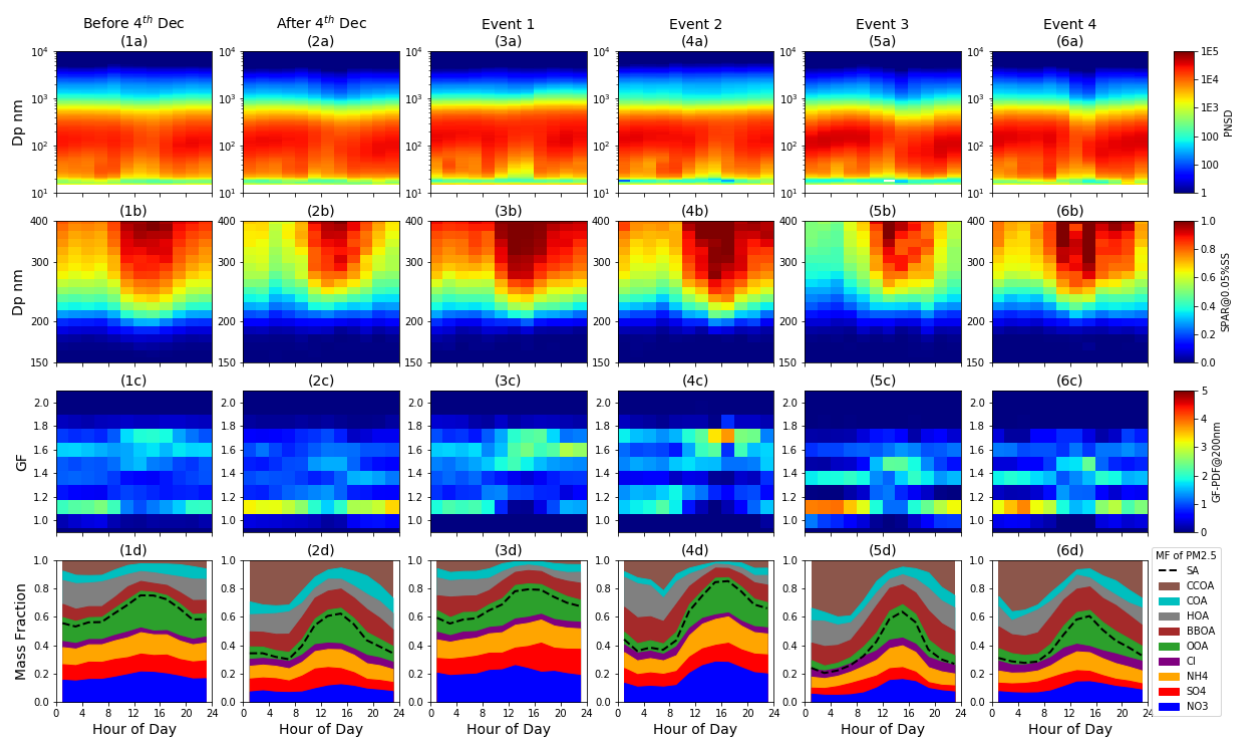
Fig 2. Diurnal variation of (a) PNSD, (b) SPAR at SS of 0.05%, (c) GF-PDF at 200 nm and (d) mass fraction of different PM$_{2.5}$ chemical species during high RH periods before 4th Dec (1), low RH periods after 4th Dec (2) and the four events (3-6), including OA factors: hydrocarbon-like OA (HOA), cooking OA (COA), biomass burning OA (BBOA), coal combustion OA (CCOA), and oxygenated OA (OOA).

941
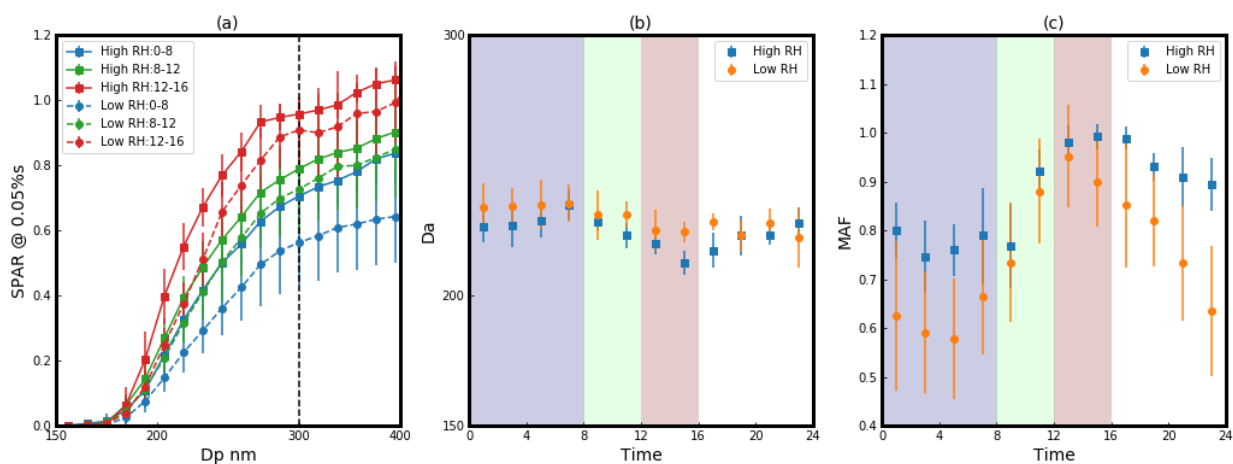
942

943   Fig 3. (a) The averages of SPAR curves at SS of 0.05% in three different time periods (blue: 0:00-

944   8:00; green: 8:00-12:00; red: 12:00-16:00) during high (squares with solid line, event 1 and 2) and low

945   (dots with dashed line, event 3 and 4) RH events. Diurnal variation of (b) D_a and (c) MAF under high

946   (blue) and low (yellow) RH conditions. The blue, green and red shades correspond to with the three

947   periods in (a & d). Error bars indicate the standard deviations of data.

948
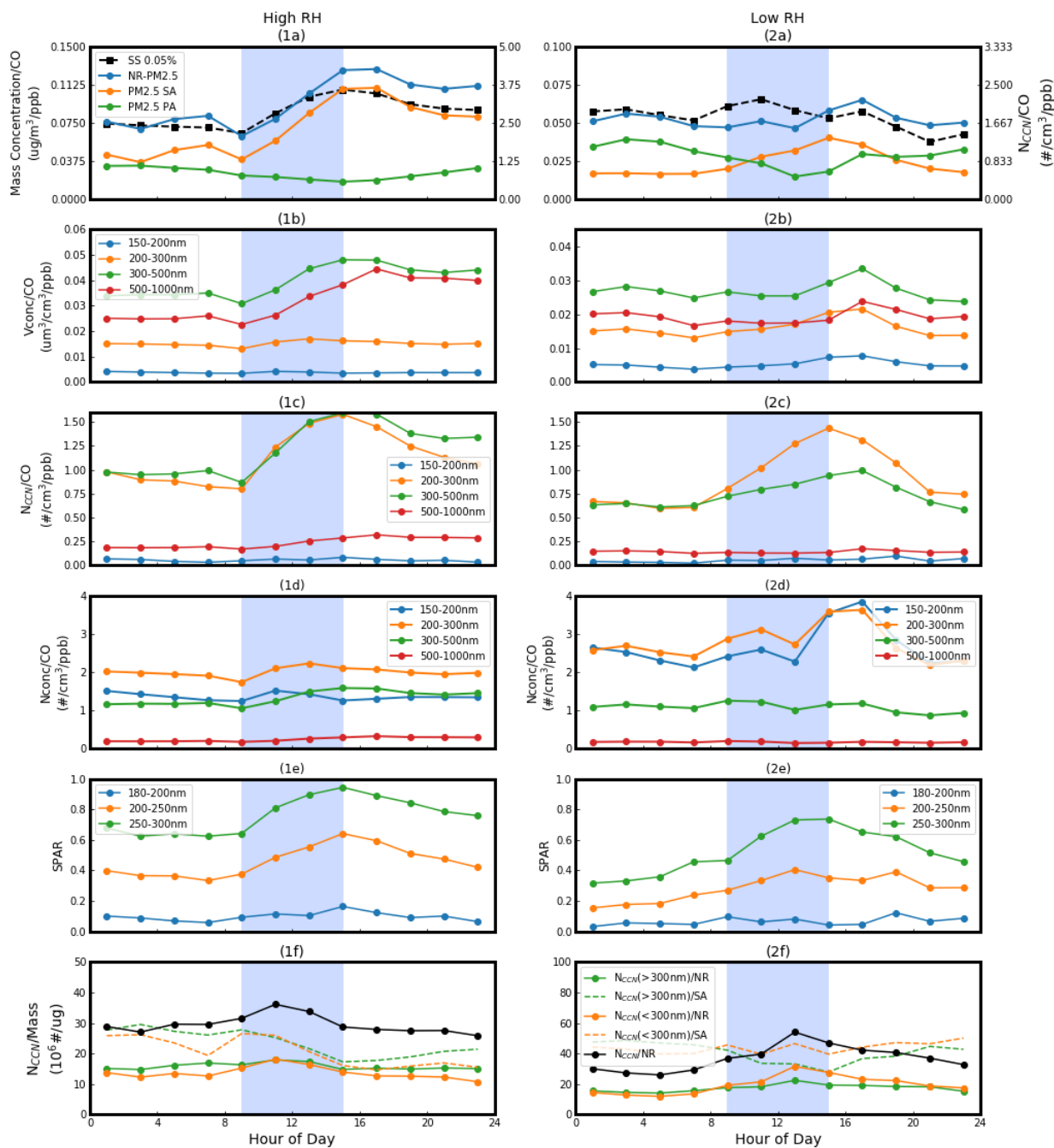
949 Fig 4. During different RH events, the average diurnal variation of (a) the ratios between particle

950 mass concentration (dots with solid lines; blue: NR-PM2.5; yellow: PM2.5 SA; green: PM2.5 PA) and

951 CO concentration, and the ratio between N_{CCN} at SS of 0.05% and CO concentration (squares with

952 solid line); (b) the ratios between particle volume concentration (Vconc) of different particle size

953 range (indicated by colors) and CO concentration; (c) the ratios between N_{CCN} of different particle

954 size range at SS of 0.05% (indicated by colors) and CO concentration; (d) the ratios between particle

955 number concentration (Nconc) of different particle size range (indicated by colors) and CO

956 concentration; (e) SPAR of different particle size range (indicated by colors); (f) the ratios between

957 N_{CCN} at SS of 0.05% (black: bulk N_{CCN}; yellow: N_{CCN} with particle size larger than 300 nm; blue:

958   N_{CCN} with particle size smaller than 300 nm) and mass concentration of NR-PM$_{2.5}$ SA and the ratios

959   between N_{CCN} and mass concentration of NR-PM$_{2.5}$ (dashed lines).

960

961
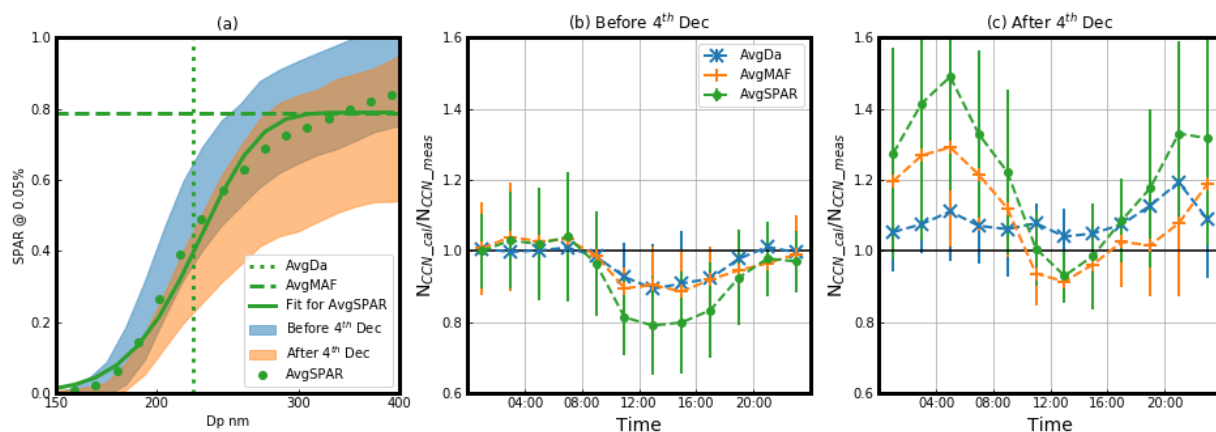
Fig 5. (a) The averaged SPAR at SS of 0.05% during the campaign (green scatters), the corresponding fitting curve (green line) and the averaged fitting parameters (dotted line for D_a and dashed line for MAF). The blue and yellow shaded areas represent the variations of SPAR before 4th Dec and after 4th Dec, respectively. The ratio between calculated N_{CCN} and measured N_{CCN} under (b) before and (c) after 4th Dec. Bars represent one standard deviation and colors represent different calculation of SPAR curves: green represent average SPAR during the campaign (AvgSPAR), yellow represent SPAR calculated with average D_a and real-time MAF (AvgDa) and blue represent SPAR calculated with average MAF and real-time D_a (AvgMAF).

970
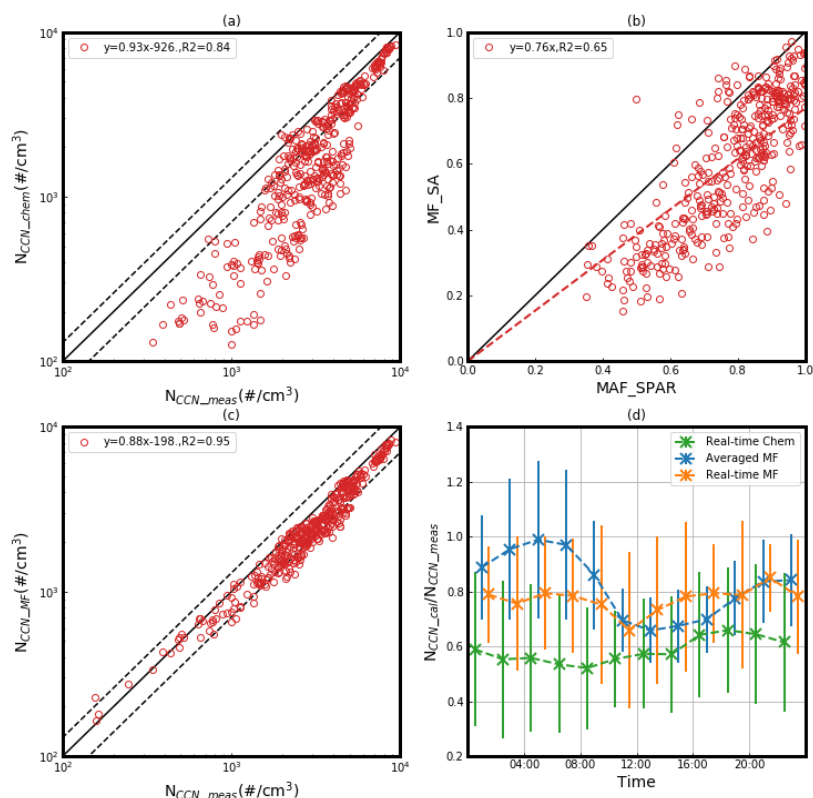
Fig 6. (a) The comparison between calculated N_{CCN} based on κ derived from bulk particle chemical compositions (N_{CCN_chem}) and measured N_{CCN} at SS of 0.05%. (b) The correlation between MAF and mass fraction of secondary aerosol (MF_{SA}). (c) the comparison between calculated N_{CCN} based on SPAR derived from real-time MF_{SA} and average D_a (N_{CCN_MF}) and measured N_{CCN}. The black dashed lines represent the relative deviation of 30%. (d) the diurnal variations of the ratio between the calculated and measured N_{CCN} during the whole campaign based on different methods (green: N_{CCN_chem}; blue: N_{CCN} calculated based on SPAR derived from averaged MF_{SA} and average D_a; yellow: N_{CCN_MF}).

979

980
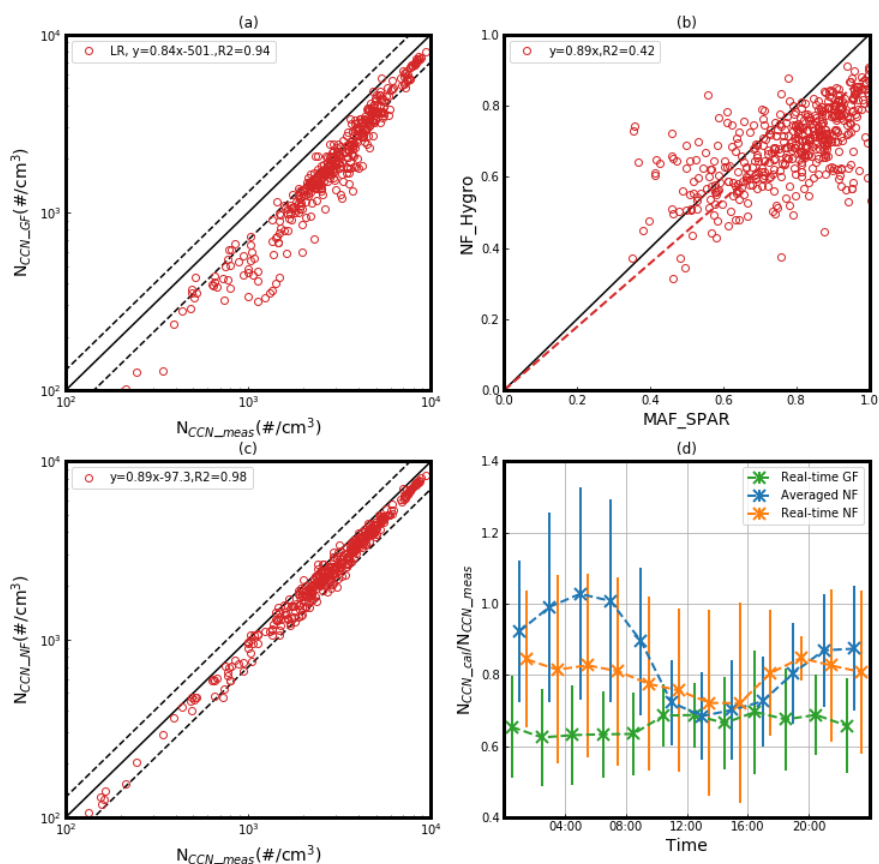
Fig 7. (a) The comparison between calculated N_{CCN} based on κ derived from bulk GF at 200 nm (N_{CCN_GF}) and measured N_{CCN} at SS of 0.05%. (b) The correlation between MAF and number fraction of hygroscopic particles (NF_{hygro}, GF>1.2). (c) The comparison between calculated N_{CCN} based on SPAR derived from real-time NF_{hygro} and average D_a (N_{CCN_NF}) and measured N_{CCN}. The black dashed lines represent the relative deviation of 30%. (d) the diurnal variations of the ratio between the calculated and measured N_{CCN} during the whole campaign based on different methods (green: N_{CCN_GF}; blue: N_{CCN} based on SPAR derived from averaged NF_{hygro} and average D_a; yellow: N_{CCN_NF}).